

Cosmic evolution of radio-excess AGNs in quiescent and star-forming galaxies across $0 < z < 4$

Yijun Wang (王倚君)^{1,2}, Tao Wang (王涛)^{1,2}, Daizhong Liu (刘岱钟)³, Mark T. Sargent,⁴ Fangyou Gao (高方宥)^{1,2}, David M. Alexander⁵, Wiphu Rujopakarn^{6,7}, Luwenjia Zhou (周陆文嘉)^{1,2}, Emanuele Daddi⁸, Ke Xu (许可)^{1,2}, Kotaro Kohno^{9,10}, Shuowen Jin (靳硕文)^{11,12}

¹ Department of Astronomy, Nanjing University, Nanjing 210093, China
e-mail: taowang@nju.edu.cn

² Key Laboratory of Modern Astronomy and Astrophysics (Nanjing University), Ministry of Education, Nanjing 210093, China

³ Max-Planck-Institut für extraterrestrische Physik, Giessenbachstrasse 1, D-85748, Garching, Germany

⁴ International Space Science Institute (ISSI), Hallerstrasse 6, CH-3012 Bern, Switzerland

⁵ Centre for Extragalactic Astronomy, Department of Physics, Durham University, South Road, Durham, DH1 3LE, UK

⁶ National Astronomical Research Institute of Thailand, Don Kaeo, Mae Rim, Chiang Mai 50180, Thailand

⁷ Department of Physics, Faculty of Science, Chulalongkorn University, 254 Phayathai Road, Pathumwan, Bangkok 10330, Thailand

⁸ CEA, IRFU, DAp, AIM, Université Paris-Saclay, Université Paris Diderot, Sorbonne Paris Cité, CNRS, F-91191 Gif-sur-Yvette, France

⁹ Institute of Astronomy, Graduate School of Science, The University of Tokyo, 2-21-1 Osawa, Mitaka, Tokyo 181-0015, Japan

¹⁰ Research Center for the Early Universe, Graduate School of Science, The University of Tokyo, 7-3-1 Hongo, Bunkyo-ku, Tokyo 113-0033, Japan

¹¹ Cosmic Dawn Center (DAWN), Copenhagen, Denmark

¹² DTU Space, Technical University of Denmark, Elektrovej 327, 2800 Kgs. Lyngby, Denmark

February 20, 2024

ABSTRACT

Context. Radio-excess active galactic nuclei (radio-AGNs) are essential to our understanding of both the physics of black hole (BHs) accretion and the interaction between BHs and host galaxies. Recent deep and wide radio continuum surveys have made it possible to study radio-AGNs down to lower luminosities and up to higher redshifts than previous studies, providing new insights into the abundance and physical origin of radio-AGNs.

Aims. Here we focus on the cosmic evolution, physical properties and AGN-host galaxy connections of radio-AGNs selected from a total sample of $\sim 400,000$ galaxies at $0 < z < 4$ in the GOODS-N and COSMOS fields.

Methods. Combining the deep radio continuum data with multi-band, de-blended far-infrared and sub-millimeter data, we are able to identify 983 radio-AGNs out of the entire galaxy sample through radio excess relative to the far-infrared-radio relation.

Results. We study the cosmic evolution of 1.4 GHz radio luminosity functions (RLFs) for both star-forming galaxies (SFGs) and radio-AGNs, which can be well described by a pure luminosity evolution of $L_{\star} \propto (1+z)^{-0.34 \times z + 3.57}$ and a pure density evolution of $\Phi_{\star} \propto (1+z)^{-0.77 \times z + 2.69}$, respectively. We derive the turnover luminosity, above which the number density of radio-AGNs surpasses that of SFGs. We show that this crossover luminosity increases as increasing redshifts, from $10^{22.9} \text{ W Hz}^{-1}$ at $z \sim 0$ to $10^{25.2} \text{ W Hz}^{-1}$ at $z \sim 4$. At full redshift range of $0 < z < 4$, we further derive the probability (p_{radio}) of SFGs and quiescent galaxies (QGs) hosting a radio-AGN, as a function of stellar mass (M_{\star}), radio luminosity (L_{R}), and redshift (z), which yields $p_{\text{radio}} \propto (1+z)^{3.08} M_{\star}^{1.06} L_{\text{R}}^{-0.77}$ for SFGs, and $p_{\text{radio}} \propto (1+z)^{2.47} M_{\star}^{1.41} L_{\text{R}}^{-0.60}$ for QGs, respectively.

Conclusions. The quantitative relation for the probabilities of galaxies hosting a radio-AGN indicates that radio-AGNs in QGs prefer to reside in more massive galaxies with larger L_{R} than those in SFGs. The fraction of radio-AGN increases towards higher redshift in both SFGs and QGs, with a more rapid increase in SFGs.

Key words. galaxies: active – galaxies: evolution – galaxies: general – galaxies: luminosity function – radio continuum: galaxies

1. Introduction

Active galactic nuclei (AGNs) are believed to play an important role in the growth of galaxies through high kinetic or radiative power (AGN feedback; Fiore et al. 2017; Matzeu et al. 2023; Fabian 2012, for a general review). AGNs emit energy across the whole spectrum, which can be identified in multiple wavelengths, including optical (Baldwin et al. 1981; Kauffmann et al. 2003; Kewley et al. 2013), mid-infrared (MIR; Lacy et al. 2004; Donley et al. 2012), X-ray (e.g., Xue et al. 2016; Luo et al. 2017), and radio bands (e.g., Del Moro et al. 2013). Approaches

through optical/MIR/X-ray surveys are sensitive to select AGNs with relatively high Eddington ratio, while selection through radio bands can find more AGNs with weak nuclear activities and help to build a more complete AGN sample (Delvecchio et al. 2017; Radcliffe et al. 2021). Radio AGNs have been found to preferentially reside in massive quiescent galaxies (QGs) (Condon & Dressel 1978; Brown et al. 2011; Vaddi et al. 2016; Ho 2008, for a general review), and in dense environments (Best et al. 2005; Worpel et al. 2013; Pasini et al. 2022). They may make a significant effect on the evolution of their host galaxies and environments through the mechanical/jet/radio mode feed-

back (Fabian 2012; Hardcastle & Croston 2020; Kondapally et al. 2023; Magliocchetti 2022, for reviews). Constructing a large and complete radio AGN sample over a broad luminosity range and a wide redshift range can greatly enlarge our understanding about their abundance and occupation fraction, and improve our knowledge about the impact AGN feedback has on host galaxies and their environments.

One effective approach to select radio-AGNs is through selecting objects with radio emission exceeding that expected from star formation, especially for less luminous radio-AGNs. In the star formation process, IR emission is expected to be correlated with radio emission due to their mutual origins from activities of massive stars (Condon 1992; Dubner & Giacani 2015), so-called IR-radio correlation (IRRC), which has been established by many observational studies (e.g. Helou et al. 1985; Condon 1992; Yun et al. 2001; Appleton et al. 2004; Ivison et al. 2010; Sargent et al. 2010a,b; Delhaize et al. 2017; Molnár et al. 2021). This IRRC can be used to identify radio AGNs (also be called as radio-excess AGNs; Donley et al. 2005; Park et al. 2008; Del Moro et al. 2013; Calistro Rivera et al. 2017), because AGNs may have extra radio emission related to nuclear activities, such as radio jets, AGN-driven outflows, and the innermost accretion disk coronal activities (Panessa et al. 2019, for a review). This method can select many AGNs that are usually missed by other established techniques, such as optical, X-rays, or MIR surveys (Park et al. 2008; Del Moro et al. 2013).

Separating radio-AGNs from SFGs requires both sensitive radio and far-infrared observations, which is particularly important for low luminosity radio-AGNs. In the local Universe, it has been known that SFGs dominate at the low radio luminosity end while AGNs constitute a significant fraction of radio populations at high luminosity end (e.g., Seymour et al. 2008; Condon et al. 2019; Franzen et al. 2021; Matthews et al. 2021). At higher redshift, however, large uncertainty remains due to the difficulty in simultaneously detecting faint and luminous objects with both IR and radio facilities (e.g., Novak et al. 2018). The situation has been significantly improved with the accomplishment of deep and wide radio surveys, e.g., the 3 GHz VLA COSMOS survey (Smolčić et al. 2017b; Novak et al. 2017; Smolčić et al. 2017a; Delvecchio et al. 2022), the Low Frequency Array Two-metre Sky Survey (LoTSS) Deep Fields (Best et al. 2023; Sabater et al. 2021; Tasse et al. 2021), and the MeerKAT International GHz Tiered Extragalactic Exploration (MIGHTEE) Survey (Jarvis et al. 2016). Moreover, even deeper VLA (Owen 2018; Alberts et al. 2020) and far-infrared surveys (Liu et al. 2018, Wang et al. in prep.) are available in the GOODS fields, these improvements greatly enlarge the radio sample with more faint objects. Furthermore, thanks to the detailed de-blended photometry for the FIR/submillimeter imaging data in the GOODS and COSMOS fields (Liu et al. 2018; Jin et al. 2018, Wang et al. in prep.), more precise estimates for the IR luminosity are available to further improve the distinction between different radio populations. Combining the power of these wide and deep surveys has great potentials to constrain the abundance and physical properties of radio-AGNs down to lower luminosities and up to higher redshifts.

In addition to the abundances of radio-AGNs, the occupation fraction of radio-AGNs in different galaxy populations is also essential to constrain models of AGN accretion and feedback. While the most luminous radio-AGNs are primarily located in massive quiescent galaxies in the local universe (e.g., Peacock & Nicholson 1991; Magliocchetti et al. 2004; Donoso et al. 2010; Worpel et al. 2013; Kolwa et al. 2019; Dullo et al. 2023), it remains unclear whether this is the case at high redshifts

(e.g., $z \sim 2$, Malavasi et al. 2015), and for the less luminous ones (Uchiyama et al. 2022). Radio luminosities of AGN may fundamentally depend on the efficiency of gas accretion onto the black hole (BH), which can be reflected in the BH fundamental plane ($L_R - L_X - M_{BH}$ relation; e.g., Merloni et al. 2003; Bonchi et al. 2013; Xie & Yuan 2017; Bariuan et al. 2022). Many works have systematically investigated the dependence of the radio-loud AGN (RL AGN) fraction on AGN radio luminosity, stellar mass (BH mass), and galaxy types of host galaxies especially in the local universe. RL-AGN fractions are found to increase with stellar mass in the local universe ($0.03 < z < 0.3$; Best et al. 2005; Sabater et al. 2019) and higher redshift (~ 2 ; Williams & Röttgering 2015). This stellar-mass dependence may decrease with redshift (from $z \sim 0.3$ to $z \sim 2$; Williams & Röttgering 2015; Zhu et al. 2023). Moreover, RL-AGN fraction may decrease with radio luminosity (Best et al. 2005; Sabater et al. 2019), and increase with redshift (Donoso et al. 2009; Zheng et al. 2022). Galaxy colors or galaxy populations have a significant effect on the RL-AGN fraction (Janssen et al. 2012; Kondapally et al. 2022), which may indicate that supermassive black hole (SMBH) are fuelled by different mechanisms in different galaxy populations (Kondapally et al. 2022). However, at higher redshift and for fainter radio-AGNs, it is still unclear about the dependence of radio-AGN fraction on diverse physical properties of galaxies. Thanks to the deeper and wider radio surveys (e.g., Smolčić et al. 2017b; Owen 2018; Alberts et al. 2020; Best et al. 2023), studying the cosmic evolution of both weak and powerful radio-AGNs has become possible, which will greatly enrich our understanding about the physical properties of radio-AGNs and their feedback. Moreover, given that different galaxy populations (e.g., SFGs and QGs) may present different associations with AGN feedback (Fiore et al. 2017; Delvecchio et al. 2022; Matzeu et al. 2023; Fabian 2012, for a general review), systematic studies about the radio AGN fractions in different galaxy populations are required to help us further understand the detailed effects of AGN feedback. In addition, most of previous studies usually estimated the AGN fraction as a function of solely stellar mass, luminosity, or redshift. To systematically investigate the possible physical properties affecting the radio activities of AGN, a unified quantitative relation describing radio-AGN fractions as a function of stellar mass, radio luminosity, and redshift is required. We may expect this unified relation to serve as an important complement for AGN feedback mode in simulations, such as IllustrisTNG (Weinberger et al. 2017; Pillepich et al. 2018) and SIMBA (Davé et al. 2019), in the future.

In this work, we firstly use the UV/optical/MIR surveys in the GOODS-N and COSMOS/UltraVISTA fields (totaling 1.55 degree^2) to construct a large galaxy sample at $0.1 < z < 4$ (Section 2). Then we cross-match this UV/optical/MIR catalog with the deep/large radio surveys and de-blended IR luminosity catalogs in these fields (Section 2). Next we calculate IR and radio luminosities for individual objects (Section 3), and use IR-radio-luminosity-ratio to select radio-excess AGNs at $0.1 < z < 4$ (Section 4). Further, we investigate the cosmic evolution and physical properties of radio-excess AGNs through the following two aspects: (1) constructing radio luminosity functions for SFGs and radio-excess AGNs, respectively, and studying their evolution with redshift (Section 5); (2) calculating the radio-excess AGN fraction as a function of stellar mass, radio luminosity, and redshift in different galaxy populations such as SFGs and QGs (Section 6). The interpretation about our results are discussed in Section 7. We summarize our conclusions in Section 8. Throughout this paper, we assume a Chabrier (2003) initial

mass function (IMF) and a flat cosmology with the following parameters: $\Omega_m = 0.3$, $\Omega_\Lambda = 0.7$, and $H_0 = 70 \text{ km s}^{-1} \text{ Mpc}^{-1}$.

2. Data and samples

Our sample is selected from two fields: the Great Observatories Origins Deep Survey North (GOODS-N; Barro et al. 2019) and the UltraVISTA survey in the Cosmic Evolution Survey (COSMOS; Scoville et al. 2007; Weaver et al. 2022). The GOODS-N survey belonging to the deep fields in the Cosmic Assembly Near-infrared Deep Extragalactic Legacy Survey (CANDELS; Grogin et al. 2011; Koekemoer et al. 2011) is suitable to study faint objects in this work. The GOODS-N field has a region size of 171 arcmin^2 , which is not large enough to detect many luminous objects. Therefore, we also use observational data from the COSMOS/UltraVISTA field with a region size of 1.5 degree^2 . The COSMOS/UltraVISTA field is within the full COSMOS field that is the largest *HST* survey imaging a 2 deg^2 field (Scoville et al. 2007; Weaver et al. 2022). Here we only use the data from the COSMOS/UltraVISTA field in order to utilize the de-blended FIR/sub-mm photometry catalog from Jin et al. (2018). In addition, the GOODS-N field has deeper radio (Owen 2018) and IR (Liu et al. 2018) surveys than the COSMOS field (Smolčić et al. 2017b; Jin et al. 2018). Therefore, summing up the data from these two fields can help us construct a large sample including both faint and luminous objects. The available multi-wavelength data and total samples from the GOODS-N and COSMOS fields in this work are summarized in Figure 1. Next we show the detailed matching processes and sample selections in each field (the overall flowchart is summarized in Figure 1).

2.1. GOODS-N field

Firstly, we collected UV-optical-MIR data in the GOODS-N field from Barro et al. (2019) (hereafter B19). This UV-optical-MIR catalog covers the wavelength range between 0.4 and $8 \mu\text{m}$, and contains 35,445 sources over 171 arcmin^2 . We selected 29,267 sources as our All Galaxies Sample according to the following two criteria: (1) $0.1 < z \leq 4.0$; (2) signal-to-noise ratio (S/N) of F160W band ≥ 5 .

Next, FIR-submillimeter-radio data in the GOODS-N field are derived from Liu et al. (2018) (hereafter L18). This FIR-submillimeter-radio catalog was established using *Spitzer* $24 \mu\text{m}$ or VLA 20 cm detected sources as priors for FIR/submm photometry which have potentially significant source confusion. This “super-deblended” photometry method provides more accurate estimates for FIR/submm flux of each individual source. This catalog contains 3306 sources with photometry at MIR (*Spitzer* 16 and $24 \mu\text{m}$), FIR (*Herschel* 100, 160, 250, 350, and $500 \mu\text{m}$), submm (SCUBA2 $850 \mu\text{m}$ and AzTEC+MAMBO $1160 \mu\text{m}$), and radio (VLA 1.4 GHz) bands. The 1.4 GHz data are primarily from Owen (2018) with rms noise (σ) in the radio image center of $2.2 \mu\text{Jy}$, supplemented by Morrison et al. (2010) with σ in the radio image center of $3.9 \mu\text{Jy beam}^{-1}$. For sources weaker than 5σ detection limit of Owen (2018), Liu et al. (2018) performed prior-extraction photometry and Monte Carlo simulations on the radio image of both Owen (2018) and Morrison et al. (2010).

Then we cross-matched the FIR-submillimeter-radio catalog (L18) with the UV-optical-MIR catalog (B19) by a match radius of 1.5 arcsec . The match radius is defined according to the average angular resolution of 1.4 GHz VLA survey in the GOODS-N field, which is 1.6 arcsec (Owen 2018). 2584 (of 3306) objects in

L18 have UV/optical/MIR counterparts in B19. The remaining 722 sources in L18 is out of the CANDELS F160W mosaic region over 171 arcmin^2 in the CANDELS/GOODS-N field, which will not be used in this work.

Finally, among the above-mentioned 2584 sources, we selected 509 sources as our Radio Sources Sample according to the following two criteria: (1) $0.1 < z \leq 4.0$; (2) S/N of 1.4 GHz radio flux ≥ 5 . The Radio Sources Sample have multi-wavelength data (UV-optical-IR-submm-radio bands) which can be used to estimate various galaxy properties (such as $8\text{--}1000 \mu\text{m}$ IR luminosity L_{TIR} and stellar mass M_\star) through broadband spectral-energy-distribution (SED) fitting with CIGALE (see details in Section 3.1).

2.2. COSMOS/UltraVISTA field

Firstly, UV-optical-MIR catalog in the COSMOS/UltraVISTA field is derived from the full COSMOS field (Weaver et al. 2022, hereafter W22). The full COSMOS survey covers the wavelength range between 0.2 and $8 \mu\text{m}$, and contains 1,720,700 sources over 2 degree^2 . The COSMOS/UltraVISTA field is within the central 1.5 degree^2 of the full COSMOS survey, which contains about 888,705 objects. From these 888,705 objects, 405,408 objects are selected as our All Galaxies Sample in the COSMOS/UltraVISTA field according to the following two criteria: (1) $0.1 < z \leq 4.0$; (2) S/N of Ks band ≥ 5 .

Next, we collected FIR-submm-radio data from Jin et al. (2018) (hereafter J18). Similar to the analysis in the GOODS-N, J18 provided a de-blended FIR (*Herschel* 100, 160, 250, 350, and $500 \mu\text{m}$) and (sub)millimeter (SCUBA2 $850 \mu\text{m}$, AzTEC 1.1 mm , and MAMBO 1.2 mm) photometric catalog for 191,624 objects in the COSMOS/UltraVISTA field. This catalog also contains observational data at *Spitzer* $24 \mu\text{m}$ band and radio detections at 3 GHz from the VLA-COSMOS 3 GHz project with an rms noise in the field center of $2.3 \mu\text{Jy beam}^{-1}$ (Smolčić et al. 2017b).

Then we cross-matched the FIR-submm-radio catalog (J18) with the UV-optical-MIR catalog (W22) by a radius of 0.5 arcsec , and 178,494 of 191,624 objects in J18 have UV/optical/MIR counterparts in W22. The match radius is defined according to the average angular resolution of 3 GHz VLA-COSMOS survey, which is 0.75 arcsec (Smolčić et al. 2017b).

Finally, among the above-mentioned 178,494 objects, we selected 7006 objects as our Radio Sources Sample in the COSMOS/UltraVISTA field according to the following two criteria: (1) $0.1 < z \leq 4.0$; (2) S/N of 3 GHz radio flux ≥ 5 .

3. Galaxy property estimation

3.1. Rest-frame $8\text{--}1000 \mu\text{m}$ IR luminosity

GOODS-N field: For 2584 objects in the GOODS-N field which have multi-wavelength data from UV to FIR/sub-mm to radio bands, we estimated the total IR luminosity from 8 to $1000 \mu\text{m}$ through spectral energy distribution (SED) fitting with Code Investigating GALaxy Emission (CIGALE 2022.0; Burgarella et al. 2005; Noll et al. 2009; Boquien et al. 2019; Yang et al. 2020, 2022). We refer readers to Appendix A for more details about the SED fitting.

COSMOS/UltraVISTA field: For sources in the COSMOS/UltraVISTA field, we use $8\text{--}1000 \mu\text{m}$ luminosity estimated by the SED fitting in J18. Their SED components consist of a stellar component from Bruzual & Charlot (2003) with a

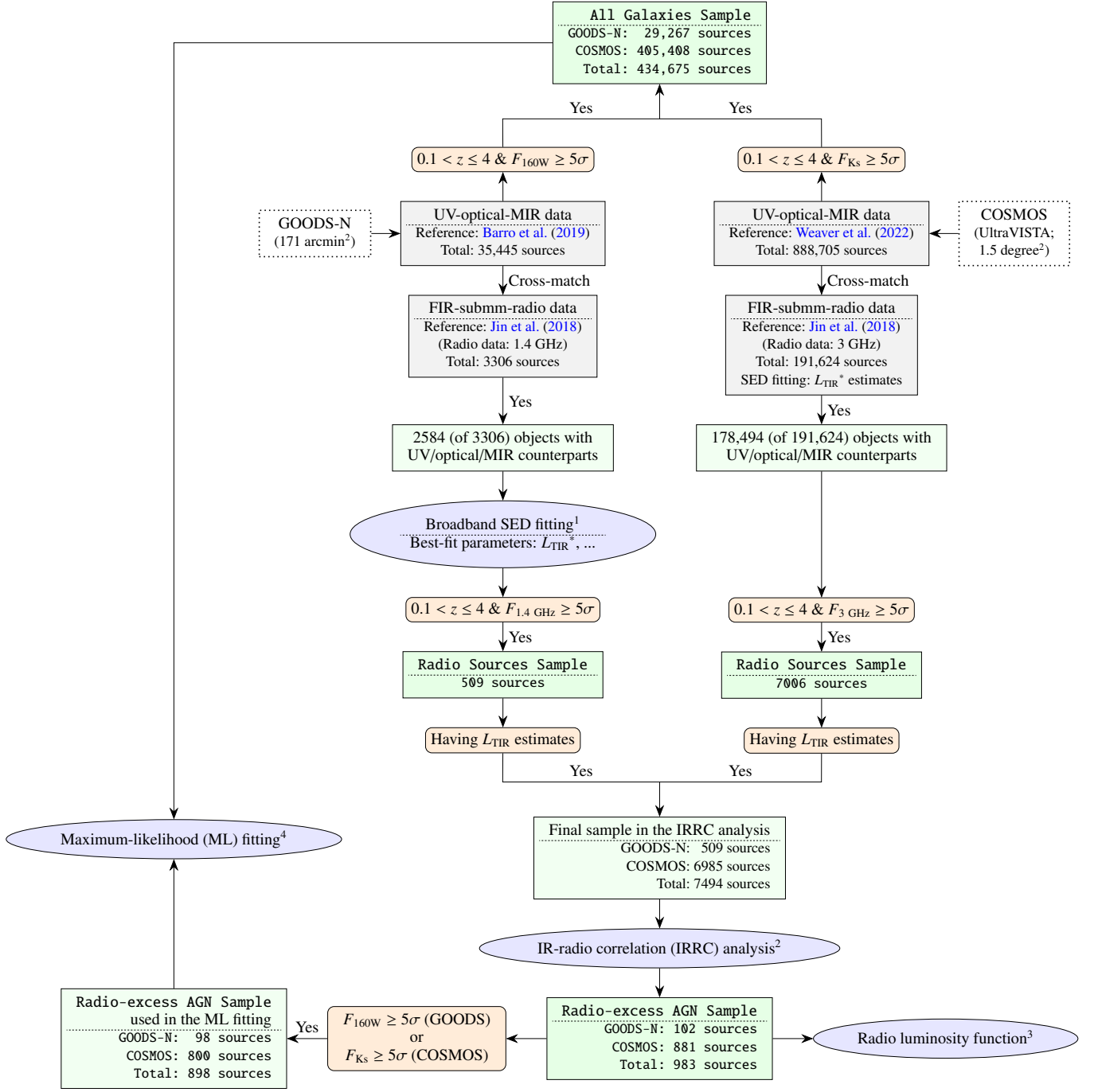


Fig. 1: Flowchart of the matching processes and sample selections (see details in Section 2). ¹ See details about broadband SED fitting in Section 3.1 and Appendix A. ² See details about IR-radio correlation (IRRC) analysis in Section 4. ³ See details about radio luminosity function in Section 5. ⁴ See details about Maximum-likelihood (ML) fitting method used for calculating the probability of hosting a radio-excess AGN in Section 6. * L_{TIR} : rest-frame total IR luminosity between 8 and 1000 μm .

Small Magellanic Cloud attenuation law, dust continuum emission based on Draine & Li (2007), a MIR AGN torus component form Mullaney et al. (2011), and a power-law radio component. In addition, our work used the same Chabrier (2003) IMF as J18.

All the objects of the Radio Sources Sample in the GOODS-N field have available IR luminosity estimates. 6985 (of 7006) objects of the Radio Sources Sample in the COSMOS/UltraVISTA field have L_{TIR} estimates from J18 ($\sim 99.7\%$). Moreover, we have verified that different methods give similar IR luminosity measurements. For example, at $0.1 < z < 1$, aver-

aged IR luminosities of galaxies with $10^{10.5} < M_{\star} < 10^{11.5} M_{\odot}$ in the GOODS-N and COSMOS/UltraVISTA fields are 3.2×10^{37} and 2.6×10^{37} W, respectively.

3.2. Rest-frame 1.4 GHz radio luminosity

Throughout this work, the radio spectrum of each radio source is assumed to follow a simple power law shape of $S_{\nu} \propto \nu^{\alpha}$, where S_{ν} is the flux density at frequency ν and α is the spectral index which is assumed to be -0.8 in this work. This simple

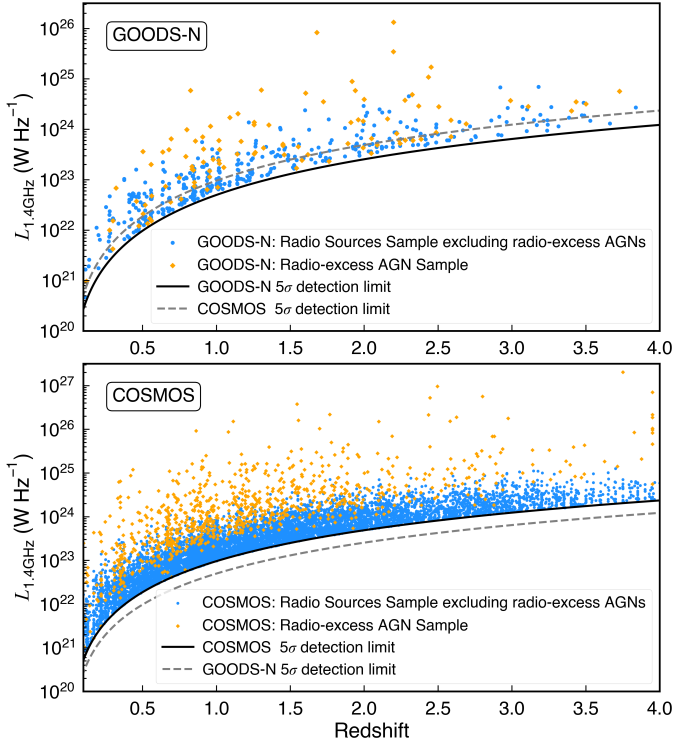


Fig. 2: Distribution of rest-frame 1.4 GHz luminosity of Radio Sources Sample (blue circles) and Radio-excess AGN Sample (orange diamonds) with redshift for the GOODS-N (top) and COSMOS/UltraVISTA (bottom) fields. The 5σ detection limit for the COSMOS/UltraVISTA field with $\sigma = 2.3 \mu\text{Jy beam}^{-1}$ at 3 GHz (Smolčić et al. 2017b) is shown as a gray dashed line in the top panel and as a black solid line in the bottom panel. The 5σ detection limit for the GOODS-N field with $\sigma = 2.2 \mu\text{Jy}$ at 1.4 GHz (Owen 2018) is shown as a black solid line in the top panel and as a gray dashed line in the bottom panel. All the detection limits are calculated by Equation 1 assuming a fixed spectral index of -0.8 (see details in Section 3.2).

power law assumed for radio spectrum is a widely used approximation due to insufficient radio data, and it is worth noting that adopting a single value of α may bring a scatter or bias to the calculation of radio luminosity (e.g., Gim et al. 2019). The rest-frame 1.4 GHz luminosity (in the unit of W Hz^{-1}) of the Radio Sources Sample can be calculated by

$$L_{1.4\text{GHz,rest}} = \frac{4\pi D_L^2}{(1+z)^{1+\alpha}} \left(\frac{1.4 \text{ GHz}}{\nu_{\text{obs}}} \right)^\alpha S_{\nu_{\text{obs}}}, \quad (1)$$

where D_L is the luminosity distance (in the unit of meter), z is the redshift, ν_{obs} is the observed frequency (in the unit of GHz), and $S_{\nu_{\text{obs}}}$ is the observed integrated flux densities at the observed frequency ν_{obs} (Ceraj et al. 2018). For the GOODS-N field, we use the observed 1.4 GHz flux to calculate the rest-frame 1.4 GHz luminosity, while for the COSMOS/UltraVISTA field, we use the observed flux at 3 GHz. We show the distribution of rest-frame 1.4 GHz luminosity of our Radio Sources Sample with redshift in Fig. 2.

3.3. Stellar mass and UVJ magnitude

For the All Galaxies Sample in the GOODS-N field, their stellar masses and rest-frame UVJ magnitudes are derived from Barro et al. (2019) where stellar masses are estimated by SED fitting with the codes FAST (Kriek et al. 2009) and Synthesizer (Pérez-González et al. 2005, 2008), and rest-frame UVJ luminosities are estimated by EAZY (Brammer et al. 2008). For the All Galaxies Sample in the COSMOS/UltraVISTA field, their stellar masses and rest-frame UVJ magnitudes are derived from Weaver et al. (2022) where stellar masses are estimated by LePhare (Arnouts et al. 2002; Ilbert et al. 2006) and rest-frame UVJ luminosities are estimated by EAZY (Brammer et al. 2008). Our work and these aforementioned works used the same Chabrier (2003) IMF. In addition, to examine whether the above different methods will bring measurement bias for stellar mass, we also compare stellar masses given by the above methods ($M_{\star}^{\text{FAST/LePhare}}$) with those obtained by the broadband SED fitting (M_{\star}^{SED} ; see details in Appendix A for the GOODS-N field and see details in Jin et al. 2018 for the COSMOS field). The logarithm of the ratio between $M_{\star}^{\text{FAST/LePhare}}$ and M_{\star}^{SED} ($\log[M_{\star}^{\text{FAST/LePhare}}/M_{\star}^{\text{SED}}]$) is around 0 ± 0.3 dex. This result indicates that different methods give a consistent measurements for stellar mass. Given that only the Radio Sources Sample and Radio-excess AGN Sample have available broadband SED fitting results while the All Galaxies Sample do not have these measures, we use the stellar mass measured by FAST or LePhare in this work.

3.4. Galaxy type: SFGs and QGs

Color-magnitude or color-color criteria are an effective method to select SFGs and QGs, which does not require accurate measurements for star formation rate and stellar mass (e.g., Williams et al. 2009). In this work, we use UVJ selection criteria in Schreiber et al. (2015) to separate all our samples into SFGs and QGs at all redshift and stellar masses:

$$\text{quiescent} = \begin{cases} U - V > 1.3 \text{ and} \\ V - J < 1.6 \text{ and} \\ U - V > 0.88 \times (V - J) + 0.49 \end{cases} \quad (2)$$

$$\text{star-forming} = \begin{cases} U - V \leq 1.3 \text{ or} \\ V - J \geq 1.6 \text{ or} \\ U - V \leq 0.88 \times (V - J) + 0.49 \end{cases} \quad (3)$$

4. Radio-excess AGN

The excess radio emission from AGNs will make these types of sources deviate from the IRRC of SFGs. Therefore, AGN activities can be identified by these excess radio emission. Following Helou et al. (1985), we define the logarithmic ratio between total IR emission (8–1000 μm ; TIR) and radio emission as

$$q_{\text{TIR}} = \log \left(\frac{L_{\text{TIR}}}{L_{1.4\text{GHz,rest}} \times 3.75 \times 10^{12} \text{ Hz}} \right), \quad (4)$$

where L_{TIR} is the total IR luminosity and $3.75 \times 10^{12} \text{ Hz}$ is the frequency at the center of FIR band ($\lambda = 80 \mu\text{m}$). In this work, we consider a broad redshift range from 0.1 to 4, which are divided into 6 redshift bins: $0.1 < z \leq 0.5$, $0.5 < z \leq 1.0$, $1.0 < z \leq 1.5$, $1.5 < z \leq 2.0$, $2.0 < z \leq 3.0$, and $3.0 < z \leq 4.0$. In

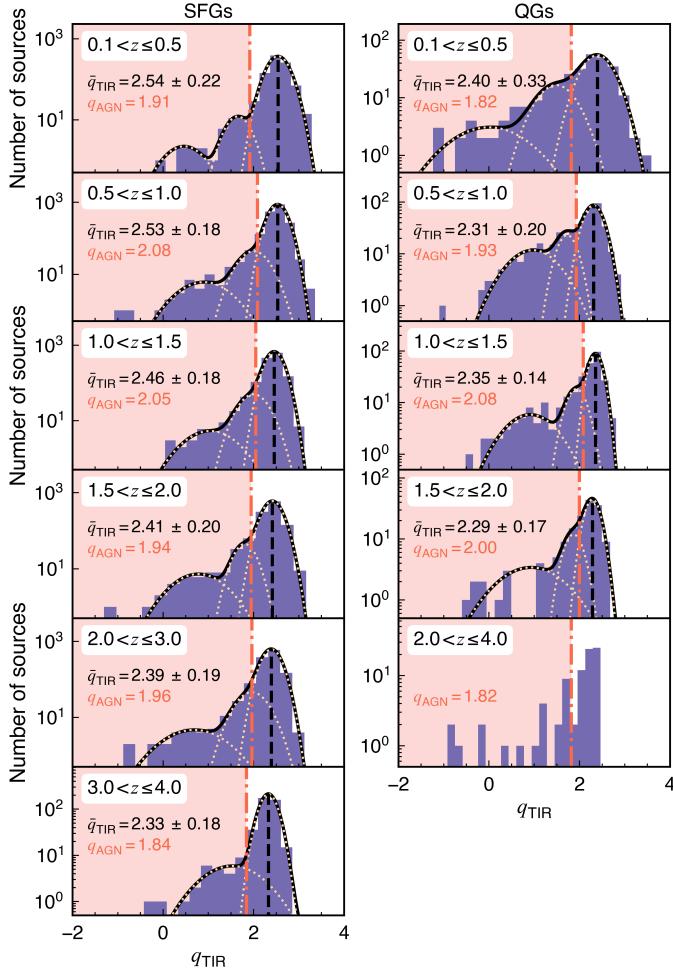


Fig. 3: Distribution of IR-radio-ratio (q_{TIR}) in SFGs (left column) and QGs (right column) at different redshift bins (from top to bottom panels). The q_{TIR} distributions are obtained by merging Radio Sources Sample from the GOODS-N and COSMOS/UltraVISTA fields together. Each yellow dotted curve represents each single gaussian model, while the black solid curve represents the best-fit model to the entire q_{TIR} distribution. The vertical black dashed line (corresponds to the \bar{q}_{TIR} value in the figure) represents the peak position of the highest gaussian component. The vertical red dash-dotted line (corresponds to the q_{AGN} value in the figure) represents the cross point between the highest gaussian component and the second highest gaussian component, which is used as the threshold to separate SFGs and radio-excess AGNs in this work. For QGs at $2.0 < z \leq 4.0$, it is difficult to find a best-fit model due to the low source number, so here we use the threshold at $0.1 < z \leq 0.5$, which does not have a significant effect to the results.

this section, we focus on the Radio Sources Sample and then use q_{TIR} distribution to select AGNs with excess radio emission which are called as radio-excess AGNs hereafter.

4.1. q_{TIR} distribution and radio-excess AGN selection

In this analysis we merge the radio sources in the GOODS-N and COSMOS/UltraVISTA fields together according to the following reasons. (1) Source numbers in each redshift bin for the GOODS-N field are small, which may result in a large uncertainty in determining the AGN selection threshold. (2) In each

redshift bin, q_{TIR} distributions in the GOODS-N and COSMOS fields have similar q_{TIR} distributions and \bar{q}_{TIR} values (see Fig. B.1). The q_{TIR} distribution consists of a gaussian component peaked at \bar{q}_{TIR} and an extended tail towards lower q_{TIR} , which is consistent with previous works (e.g., Del Moro et al. 2013). The gaussian component is attributed to the IRRC of SFGs, while the extended tail is thought to be associated with the extra radio emission from AGN. Therefore, to ensure the same selection criteria and reduce the uncertainty of the AGN selection threshold, we combine the data from the two fields together. The consistent radio luminosity functions among these two fields also indicate that our selection method is plausible (see details in Section 5). Next we analyze the q_{TIR} distribution in SFGs and QGs, respectively.

The entire q_{TIR} distribution can be described by multiple gaussian models (see the yellow dotted curves in Fig. 3). We used f -test probability at $\geq 95\%$ confidence level to decide how many models are required. The final best-fit model are shown in Fig. 3 with black solid curves. As we mentioned before, the highest gaussian peak and the extended low- q_{TIR} tail are thought to be contributed by SFGs and AGNs, respectively. Therefore, here we define the cross point between the highest gaussian and the second highest gaussian components as the threshold to separate the SFGs and radio-excess AGNs (see the q_{AGN} values and red dash-dotted lines in Fig. 3). It means that a radio source will be selected as a radio-excess AGN if its q_{TIR} value is lower than this cross point (q_{AGN}). It is worth noting that the q_{TIR} distributions of QGs also show a highest peak similar to SFGs. However, QGs are not expected to have this peak due to little or no star formation. One possible reason may be that UVJ color selection might classify part of massive SFGs with relatively lower star formation rate (SFR) as QGs (Popesso et al. 2023). We also found that nearly half of UVJ-selected QGs (without AGN) in the Radio Sources Sample locate very close to the dividing line in the UVJ diagram, which indicates that UVJ selection might not accurately classify these sources. In addition, it is worth noting that QGs in the All Galaxies Sample do not show such a distribution in the UVJ diagram. Therefore, another possible reason may be that radio detection favors sources with higher star formation, even among QGs. Radio-excess AGNs hosted by QGs do not show a prominent populations close to the dividing line in the UVJ diagram, which may be due to that radio-excess AGNs are selected by a threshold (q_{AGN}) that is significantly lower than the mean q_{TIR} of SFGs. This may explain why QGs show a highest q_{TIR} peak in Fig. 3. In addition, the difference between the second highest and the third highest gaussian component in the q_{TIR} distribution might be associated with different types of radio AGNs, which is beyond the scope of this work and will be studied in our future works.

Finally, we selected 983 radio-excess AGNs at $0.1 < z \leq 4$ as our Radio-excess AGN Sample which contains 102 sources in the GOODS-N field and 881 sources in the COSMOS/UltraVISTA field (see Fig. 2).

4.2. q_{TIR} evolution

As Fig. 4 shows, \bar{q}_{TIR} presents a weak evolution with redshift, which is in the form of

$$\bar{q}_{\text{TIR}} = (2.62 \pm 0.08) \times (1 + z)^{-0.08 \pm 0.03}. \quad (5)$$

Our result is almost consistent with previous works (see Fig. 4; Bell 2003; Magnelli et al. 2015; Delhaize et al. 2017; Novak et al. 2017; Enia et al. 2022). Bell (2003) obtained q_{TIR} value for

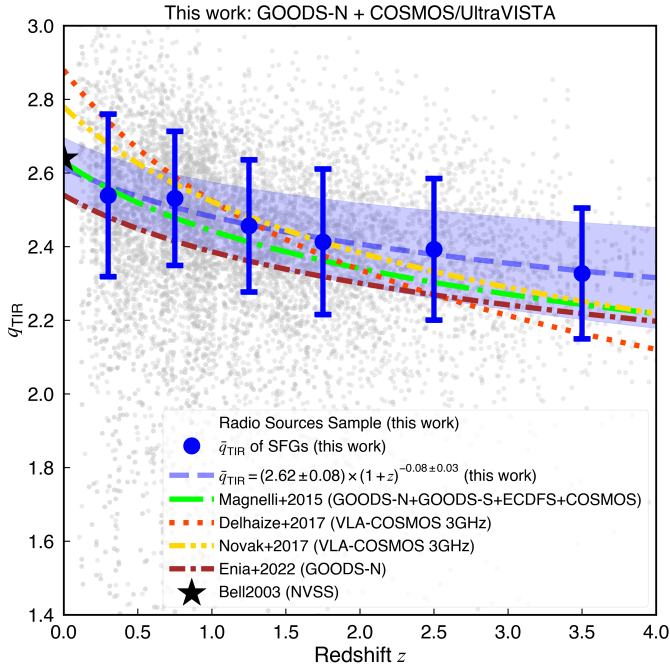


Fig. 4: The distribution of q_{TIR} with redshift. The gray points show the Radio Sources Sample in the GOODS-N and COSMOS/UltraVISTA fields (see details in Section 2). The blue points represent the \bar{q}_{TIR} values of SFGs which are shown in Fig. 3 and in Section 4.1. The blue dashed line represents the best-fit model to the data of SFGs, while the shaded blue region is the associated 1σ uncertainty of the best-fit model. The green dash-dotted line represents the best-fit model from Magnelli et al. (2015) using data in the GOODS-N, GOODS-S, ECDFS, and COSMOS fields. Both the red dotted line (Delhaize et al. 2017) and yellow dash-dotted line (Novak et al. 2017) represent the best-fit model obtained with the VLA-COSMOS 3 GHz project but using different source selection criteria. The dark-red dash-dotted line represents the best-fit model from Enia et al. (2022) based on data from the GOODS-N field. The black star represents the q_{TIR} value for SFGs in the local universe from Bell (2003).

SFGs in the local universe. Magnelli et al. (2015) combined data from multiple fields of the GOODS-N, GOODS-S, ECDFS, and COSMOS up to $z \sim 2$ with rms noises larger than $3.9 \mu\text{Jy}$ at 1.4 GHz. Delhaize et al. (2017) and Novak et al. (2017) both used the VLA-COSMOS 3 GHz project but used different source selection criteria. Enia et al. (2022) focused on SFGs in the GOODS-N field. Compared to their works, we use simultaneously deeper and larger radio surveys, and more precise IR luminosity based on de-blended IR photometry. The slight difference between our results and previous works might be due to the different selection method for sources. In addition, the averaged standard deviation (1σ error of q_{TIR} in Fig. 4) of q_{TIR} distribution for SFGs is around 0.18 which is consistent with the previous works (e.g., Del Moro et al. 2013).

More recently, Delvecchio et al. (2021) found that the IRRC of SFGs strongly depends on stellar mass (M_*), while An et al. (2021) found a weak dependence. To examine whether considering M_* -dependence or not affects our results, we make some simple tests. For the Radio Sources Sample in the COSMOS/UltraVISTA field, at $0.1 < z < 1$, \bar{q}_{TIR} is around 2.55 and 2.53 for low-mass ($10^{10} < M_* < 10^{10.5} M_\odot$) and high-mass

($10^{10.5} < M_* < 10^{11} M_\odot$) SFGs, respectively. For the Radio Sources Sample in the GOODS-N field, at $0.1 < z < 1$, \bar{q}_{TIR} is around 2.56 and 2.51 for low-mass ($10^{10} < M_* < 10^{10.5} M_\odot$) and high-mass ($10^{10.5} < M_* < 10^{11} M_\odot$) SFGs, respectively. These results indicate that for our samples, \bar{q}_{TIR} of SFGs shows no significant dependence on stellar mass within the uncertainties of q_{TIR} . Therefore, disregarding the M_* -dependent IRRC may have no significant effect on our results.

5. Radio luminosity function and their cosmic evolution

In this section, we will construct radio luminosity function (RLF) for SFGs and radio-excess AGNs which are separated in Section 4. Firstly, we estimate the combined 1.4 GHz RLF from the GOODS-N and COSMOS/UltraVISTA fields in Section 5.1. We then show the fitting procedures and results for the evolution of SFG RLFs (see Section 5.2) and AGN RLFs (see Section 5.3), respectively. In this work we do not consider the star-formation contamination for the 1.4 GHz radio luminosity of AGN. We have verified that for most of our Radio-excess AGN Sample, radio luminosity from the star formation is not significant compared to luminosity from AGN.

5.1. Construct RLF out to $z \sim 4$

Using the $1/V_{\text{max}}$ method (Schmidt 1968), RLF in each 1.4 GHz luminosity bin and each redshift bin is calculated by

$$\Phi(L, z) = \frac{1}{\Delta \log L} \sum_i \frac{1}{\frac{\Omega}{4\pi} \times V_{\text{max},i} \times w_i}, \quad (6)$$

where $\Delta \log L$ is the size of the 1.4 GHz luminosity bin, Ω is the observed area (171 arcmin^2 for the GOODS-N field, and 1.5 degree^2 for the COSMOS/UltraVISTA field), $V_{\text{max},i}$ is the co-moving volume of the i th source that is defined as $V_{\text{max},i} = V_{z_{\text{max},i}} - V_{z_{\text{min},i}}$, and w_i is the completeness and bias correction factor of the i th source. Further, $V_{z_{\text{max},i}}$ is the co-moving volume at the maximum redshift where the i th source can be observed given the 1.4 GHz flux detection limit (the maximum value of z_{max} is equal to the upper limit of each redshift bin) and $V_{z_{\text{min},i}}$ is the co-moving volume at the lower boundary of each redshift bin. The parameter w_i is the flux density completeness of our catalogs which takes into account the effects of sensitivity limit. The completeness and bias corrections of the COSMOS and GOODS-N fields are derived from Smolčić et al. (2017b) and Enia et al. (2022), respectively, which are estimated by Monte Carlo simulations where mock sources are inserted in and retrieved from the mosaic. The uncertainty of RLF in each luminosity bin and each redshift bin can be defined as

$$\sigma_\Phi(L, z) = \frac{1}{\Delta \log L} \sqrt{\sum_i \left(\frac{1}{\frac{\Omega}{4\pi} \times V_{\text{max},i} \times w_i} \right)^2}, \quad (7)$$

We used Equations 6 and 7 to calculate RLFs and their uncertainties for the sources in the GOODS-N and COSMOS/UltraVISTA, respectively (see Fig. C.1). For both SFGs and radio-excess AGNs, RLFs in these fields present generally consistent results. At the faintest end of the lowest redshift bin ($0.1 < z \leq 0.5$), SFG RLF of the COSMOS/UltraVISTA field presents a slight decline comparing to that of the GOODS-N field (see Figure C.1). This may be due to that the higher spatial resolution of the radio survey in the COSMOS/UltraVISTA field (see details in Section 2) results in more flux losses for the extended

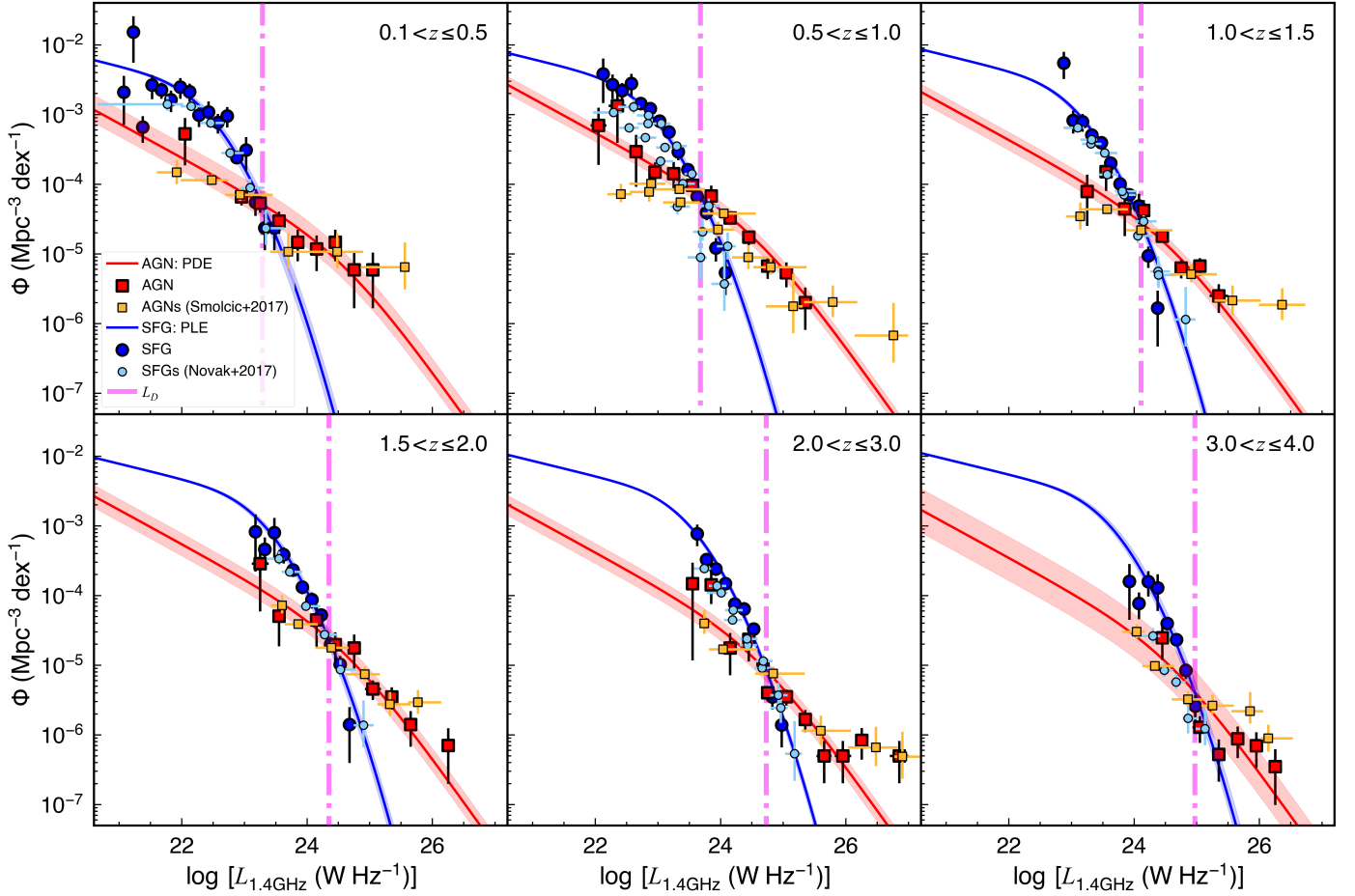


Fig. 5: The 1.4 GHz radio luminosity function of SFGs (blue circles) and radio-excess AGNs (red squares) in different redshift bins. For SFGs, blue solid line represents the best-fit PLE model which is the best model to describe the data in this work. For radio-excess AGNs, red solid line represents the best-fit PDE model which is the best model to describe the data. The magenta vertical dash-dotted line represents the turnover luminosity between the radio luminosity function of SFGs and radio-excess AGNs (see details in Section 5.4). The light-sky-blue circles show the results for SFGs from the VLA-COSMOS 3 GHz project (Novak et al. 2017) while the gold squares show the results for radio AGNs from the VLA-COSMOS 3 GHz project (Smolčić et al. 2017a). It is worth noting that we use different definition for redshift bins comparing to both Novak et al. (2017) and Smolčić et al. (2017a) especially for the highest redshift bin.

sources especially for the faint populations at low redshift. In order to well constrain the RLFs, in the following sections we use the averaged SFG RLFs in the GOODS-N and COSMOS/UltraVISTA fields, and use the averaged AGN RLFs in the two fields to make further analysis (see Fig. 5). In addition, we also correct the classification purity for the radio-excess AGN in these three fields (see details in Section B).

5.2. Fit the evolution of the SFG RLF

We assume a modified-Schechter function (Saunders et al. 1990; Smolčić et al. 2009; Gruppioni et al. 2013; Novak et al. 2017) to describe the SFG RLF. The local RLF of SFGs (Novak et al. 2017) is defined as

$$\Phi_0^{\text{SFG}}(L) = \Phi_{\star,0} \left(\frac{L}{L_{\star,0}} \right)^{1-\alpha} \exp \left[-\frac{1}{2\sigma^2} \log^2 \left(1 + \frac{L}{L_{\star,0}} \right) \right], \quad (8)$$

where $L_{\star,0} = 1.85 \times 10^{21} \text{ W Hz}^{-1}$ is the turnover position of the local SFG RLF, $\Phi_{\star,0} = 3.55 \times 10^{-3} \text{ Mpc}^{-3} \text{ dex}^{-1}$ is the local turnover normalization, and $\alpha = 1.22$ and $\sigma = 0.63$ are used to fit the distribution in the faint and bright ends, respectively.

SFG RLFs have been shown to evolve with redshift (e.g., Novak et al. 2017; Ocran et al. 2020; Cochrane et al. 2023). Given that it is difficult to simultaneously constrain the evolutions of all the parameters, we fix the α and σ at all cosmic times to those of the local RLF (Novak et al. 2017) in the fit. It means that we assume an unchanged RLF shape at all cosmic times, and only allow the turnover position (L_{\star}) and turnover normalization (Φ_{\star}) to change with redshift. In reality, α and σ might change with redshift.

Both L_{\star} evolution and Φ_{\star} evolution can be described by a simple power law:

$$L_{\star} = (1+z)^{\alpha_L} \times L_{\star,0} \quad (9)$$

and

$$\Phi_{\star} = (1+z)^{\alpha_D} \times \Phi_{\star,0}, \quad (10)$$

respectively. Therefore, the redshift-evolved SFG RLF (luminosity and density evolution; hereafter “LDE”) is defined as

$$\Phi_{\text{LDE}}^{\text{SFG}}(L, z, \alpha_L, \alpha_D) = (1+z)^{\alpha_D} \times \Phi_0^{\text{SFG}} \left(\frac{L}{(1+z)^{\alpha_L}} \right), \quad (11)$$

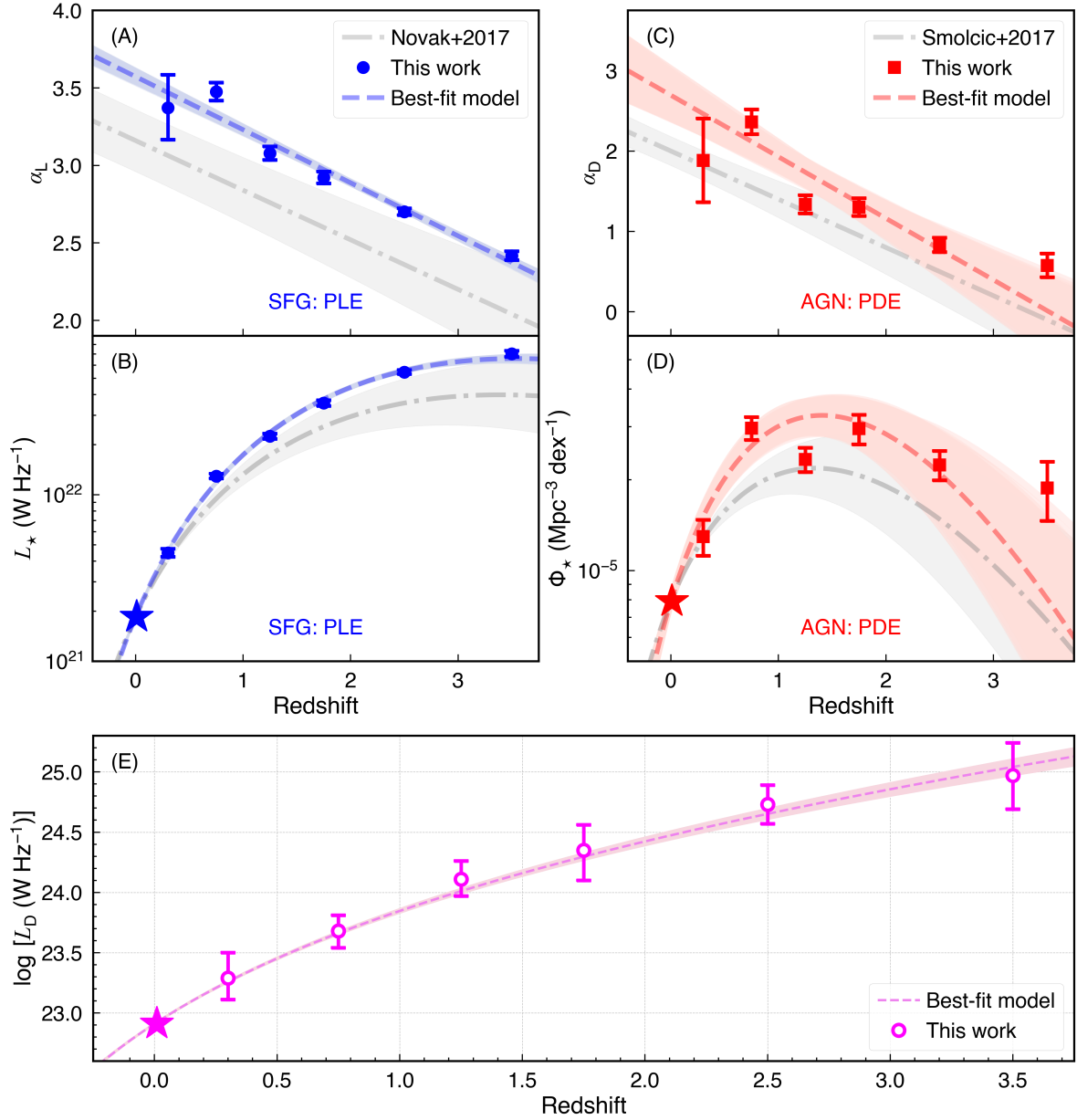


Fig. 6: Evolution of the best-fit parameters for the 1.4 GHz radio radio luminosity function (RLF) with redshift: evolution parameter (α_L) of the pure luminosity evolution (PLE) for SFGs (*Panel A*), turnover position (L_*) of the PLE for SFGs which is calculated by Equation 9 (*Panel B*), evolution parameter (α_D) of the pure density evolution (PDE) for radio-excess AGN (*Panel C*), turnover normalization (Φ_*) of the PDE for radio-excess AGN which is calculated by Equation 10 (*Panel D*), turnover luminosity (L_D) above which the number density of radio-AGNs surpasses that of SFGs (L_D) (*Panel E*). The gray dash-dotted lines in Panels A and B represent the results for SFGs from Novak et al. (2017), while the gray regions represent the corresponding 1- σ uncertainty. The gray dash-dotted lines in Panels C and D represent the results for radio-excess AGNs from Smolčić et al. (2017a), while the gray regions represent the corresponding 1- σ uncertainty. The stars in Panels B and D represent the local values obtained by Novak et al. (2017) and Mauch & Sadler (2007), respectively. The magenta star in Panel E represents the local L_D obtained by the cross point between the local SFGs RLF from Novak et al. (2017) and the local AGN RLF from Mauch & Sadler (2007). The best-fit values for α_L , α_D , L_* , Φ_* , and L_D are summarized in Table 1.

where α_D is the parameter of pure density evolution (hereafter “PDE”; vertical shift of RLF), α_L is the parameter of pure luminosity evolution (hereafter “PLE”; horizontal shift of RLF), and $\Phi_0^{\text{SFG}}(L)$ is the local SFG RLF given by Eq. 8. If we assume that there is no evolution with redshift for Φ_* and only L_* evolves

with redshift ($\alpha_D = 0$), we can define a SFG PLE model as

$$\Phi_{\text{PLE}}^{\text{SFG}}(L, z, \alpha_L) = \Phi_0^{\text{SFG}}\left(\frac{L}{(1+z)^{\alpha_L}}\right). \quad (12)$$

Similarly, SFG PDE model only allows Φ_* to evolve with redshift ($\alpha_L = 0$), which is defined as

$$\Phi_{\text{PDE}}^{\text{SFG}}(L, z, \alpha_D) = (1+z)^{\alpha_D} \times \Phi_0^{\text{SFG}}(L). \quad (13)$$

Then we used the Markov chain Monte Carlo (MCMC) algorithm in the Python package `emcee` (Foreman-Mackey et al. 2013) to fit the data (see Table D.1) with the above three models. The averaged reduced χ^2 over all the redshift bins of the best-fit LDE, PLE, and PDE models are 3.9, 4.8, and 526.4, respectively. Firstly, we ignored the PDE model because it has the worst fit to the observational data. The best-fit LDE and PLE models show significant differences at higher redshift ($z \gtrsim 1.5$) where our data points only sample the bright end of RLF. This will result in degeneracy in estimation of α_D and α_L , preventing a precise calculation to the turnover position and turnover normalization. Therefore, for simplicity, we only consider the PLE model (see Equation 12) here.

The best-fit α_L of the PLE model in each redshift bin is summarized in Table 1. α_L shows an evolution with redshift, which can be described by $\alpha_L = A_L \times z + B_L$. We obtain the best-fit results with $A_L = -0.34 \pm 0.01$ and $B_L = 3.57 \pm 0.01$ (see Panel A of Fig 6), which are also summarized in Table 1. The turnover position L_\star is estimated by Equation 9, which is also listed in Table 1. Our results are generally consistent with those in Novak et al. (2017) with the VLA-COSMOS 3 GHz project (see Fig. 5 and Fig. 6), although our results show a slightly larger B_L (see Panel A of Fig. 6) and a slightly larger L_\star (see Panel B of Fig. 6), which may be due to the different selection criteria adopted for radio SFGs. Novak et al. (2017) separated the entire radio sources sample into SFGs and radio-excess AGNs subsets, while we firstly separate our entire radio sources sample into SFGs and QGs according to the UVJ selection criteria, and further distinguish the radio-excess AGNs from them.

5.3. Fit the evolution of the AGN RLF

The AGN RLF can be assumed as a double power-law shape (Mauch & Sadler 2007). The local RLF of AGN (Mauch & Sadler 2007) is defined as

$$\Phi_0^{\text{AGN}}(L) = \frac{\Phi_{\star,0}}{(L_{\star,0}/L)^\alpha + (L_{\star,0}/L)^\beta}, \quad (14)$$

where $\Phi_{\star,0} = \frac{1}{0.5} 10^{-5.5} \text{ Mpc}^{-3} \text{ dex}^{-1}$ is the turnover normalization of the local AGN RLF, $L_{\star,0} = 10^{24.59} \text{ W Hz}^{-1}$ is the local turnover position, $\alpha = -1.27$ and $\beta = -0.49$ are the indices at the bright and faint end, respectively.

Similar to the SFG RLF, we assume that AGN RLF has an unchanged shape at all cosmic times. Thus, similar to Equations 11 – 13, LDE, PLE, and PDE models to describe AGN RLFs can be defined as

$$\Phi_{\text{LDE}}^{\text{AGN}}(L, z, \alpha_L, \alpha_D) = (1+z)^{\alpha_D} \times \Phi_0^{\text{AGN}}\left(\frac{L}{(1+z)^{\alpha_L}}\right), \quad (15)$$

$$\Phi_{\text{PLE}}^{\text{AGN}}(L, z, \alpha_L) = \Phi_0^{\text{AGN}}\left(\frac{L}{(1+z)^{\alpha_L}}\right), \quad (16)$$

$$\Phi_{\text{PDE}}^{\text{AGN}}(L, z, \alpha_D) = (1+z)^{\alpha_D} \times \Phi_0^{\text{AGN}}(L), \quad (17)$$

respectively. We also use the `emcee` package to fit the observational data for radio-excess AGNs (see Table D.2) with these three models. The averaged reduced χ^2 over all the redshift bins of the best-fit LDE, PDE, and PLE models are 2.3, 2.2, and 2.5, respectively. Here we only consider the PDE model (see Equation 16) which has the best fit to the data.

The best-fit α_D of the PDE model in each redshift bin is summarized in Table 1, which also shows a redshift evolution in a form of $\alpha_D = A_D \times z + B_D$. The best-fit A_D and B_D are -0.77 ± 0.06 and 2.69 ± 0.09 , respectively (also see Table 1). As we assumed an unchanged AGN RLF shape and a pure density evolution, the evolution of Φ_\star (calculated by Equation 10) with redshift can simply represent the number density distribution of AGN, which peaked at $z \sim 1.5$ (see Panel D of Fig. 6). Our result is generally consistent with that in Smolčić et al. (2017a) based on the VLA-COSMOS 3 GHz project (see Fig. 5 and Fig. 6), and consistent with the AGN accretion rate density history obtained with X-ray surveys (Aird et al. 2010, and references therein).

We also study the RLF of the Radio-excess AGN Sample hosted by different galaxy populations (SFGs and QGs; see Fig. E.1). At $z < 1$, the radio-excess AGN population is mainly dominated by the sources hosted by QGs, while radio-excess AGNs hosted by SFGs only have a comparable space densities at the faint end. At $z > 1$, the space densities of radio-excess AGNs hosted by QGs decrease towards higher redshift, while radio-excess AGNs hosted by SFGs show an opposite evolution trend. In addition, radio-excess AGNs hosted by SFGs completely dominate those hosted by QGs at $z > 1.5$. These trends are consistent with those for low-excitation radio galaxies (LERGs) in Kondapally et al. (2022). LERGs in Kondapally et al. (2022) are defined as objects showing powerful radio emission from AGN but not identified in other bands (e.g., IR and X-ray), which represent 89% of their entire radio-excess AGNs (11% for high-excitation radio galaxies). For our radio-excess AGNs, nearly 80% of objects do not have X-ray detections or have intrinsic 2–10 keV X-ray luminosity lower than $10^{42} \text{ erg s}^{-1}$. Our radio-excess AGNs may be otherwise identified by IR or other methods, so LERG fraction in our Radio-excess AGN Sample is expected to be lower than 80% while the fraction of high-excitation radio galaxies (HERGs) will be higher than 20%. In this work, our Radio-excess AGN Sample includes both LERGs and HERGs subsets, while Kondapally et al. (2022) mainly focused on LERGs. Even so, both of their work and our work found that radio AGNs in SFGs and QGs have significantly different cosmic evolution. Given that SFGs and QGs may have different fuelling mechanisms towards central SMBHs (e.g., Kauffmann & Heckman 2009; Kondapally et al. 2022; Ni et al. 2023), these results indicate that the radio activities of central engines may depend on the fuelling mechanisms of their host galaxies. In Section 6, we will further investigate this topic through studying the probability of radio-excess AGNs hosted by different galaxy populations.

5.4. Crossover luminosity between SFG RLF and AGN RLF

The comparison between the SFG RLF and AGN RLF shows that AGNs will dominate the radio populations beyond a certain luminosity (hereafter turnover luminosity L_D ; see the magenta dash-dotted lines in Fig. 5). In the local universe, this crossover luminosity is around $10^{23} \text{ W Hz}^{-1}$, which is usually used to select RL AGNs (e.g., Best et al. 2005; Kukreti et al. 2023). Towards higher redshift, given that both SFG RLFs and AGN RLFs show evolutions with redshift, this crossover luminosity will not be expected to be constant at all cosmic time. Our results indicate that the redshift evolution of this crossover luminosity can be described by

$$L_D = L_{D,0} \times (1+z)^{\alpha_{LD}}, \quad (18)$$

where $L_{D,0}$ is the crossover luminosity in the local universe, α_{LD} is the evolution index of the crossover luminosity. Here, $L_{D,0} =$

Table 1: Best-fit evolution parameters of radio Luminosity function for SFGs and radio-excess AGNs.

Redshift bin	SFG (PLE)		Radio-excess AGN (PDE)		
	α_L	$\log L_\star$ [W Hz ⁻¹]	α_D	$\log \phi_\star$ [Mpc ⁻³ dex ⁻¹]	$\log L_D$ [W Hz ⁻¹]
$0.1 < z \leq 0.5$	3.37 ± 0.21	21.65 ± 0.02	1.88 ± 0.52	-4.89 ± 0.06	23.29 ± 0.20
$0.5 < z \leq 1.0$	3.48 ± 0.06	22.11 ± 0.01	2.36 ± 0.15	-4.53 ± 0.04	23.68 ± 0.13
$1.0 < z \leq 1.5$	3.08 ± 0.04	22.35 ± 0.02	1.34 ± 0.11	-4.63 ± 0.04	24.11 ± 0.14
$1.5 < z \leq 2.0$	2.92 ± 0.04	22.55 ± 0.02	1.30 ± 0.11	-4.53 ± 0.05	24.35 ± 0.23
$2.0 < z \leq 3.0$	2.70 ± 0.02	22.74 ± 0.01	0.83 ± 0.09	-4.65 ± 0.05	24.73 ± 0.16
$3.0 < z \leq 4.0$	2.42 ± 0.03	22.85 ± 0.02	0.58 ± 0.15	-4.73 ± 0.10	24.97 ± 0.28
Relation	$L_\star = L_{\star,0} \times (1+z)^{\alpha_L}$ $\alpha_L = A_L \times z + B_L$		$\phi_\star = \phi_{\star,0} \times (1+z)^{\alpha_D}$ $\alpha_D = A_D \times z + B_D$		$L_D = L_{D,0} \times (1+z)^{\alpha_{LD}}$ $\alpha_{LD} = C \times z + D$
Best-fit parameters	$A_L = -0.34 \pm 0.01$ $B_L = 3.57 \pm 0.01$		$A_D = -0.77 \pm 0.06$ $B_D = 2.69 \pm 0.09$		$C = 0.06 \pm 0.01$ $D = 3.05 \pm 0.02$

Notes. For SFGs, $L_{\star,0} = 1.85 \times 10^{21}$ W Hz⁻¹, represents the turnover position of the local SFG RLF (Novak et al. 2017). For radio-excess AGNs, $\Phi_{\star,0} = \frac{1}{0.5} 10^{-5.5}$ Mpc⁻³ dex⁻¹, represents the turnover normalization of the local AGN RLF (Mauch & Sadler 2007). The local turnover luminosity $L_{D,0} = 10^{22.9}$ W Hz⁻¹, is obtained by the cross point between the local SFG RLF (Novak et al. 2017) and the local AGN RLF (Mauch & Sadler 2007).

$10^{22.9}$ W Hz⁻¹, is obtained by the cross point between the local SFG RLF (Novak et al. 2017) and local AGN RLF (Mauch & Sadler 2007). Further, α_{LD} also shows a weak evolution with redshift:

$$\alpha_{LD} = (0.06 \pm 0.01) \times z + (3.05 \pm 0.02). \quad (19)$$

These results provide us another way to select powerful radio AGNs at different redshift through solely radio survey. It means that if IR data are not available, a radio source at redshift z can be selected as a radio AGN when its 1.4 GHz radio luminosity is larger than $L_D = 10^{22.9} \times (1+z)^{0.06 \times z + 3.05}$ W Hz⁻¹. This crossover luminosity describes a luminosity threshold where radio-AGNs begin to dominate entire radio population. This result is also consistent with those from previous works (e.g., McAlpine et al. 2013), and also consistent with the radio luminosity threshold proposed for radio-AGN selection in the past (e.g., Magliocchetti et al. 2017).

6. The probability of hosting a radio-excess AGN in SFGs and QGs

In this section, we aim to study the probability of different galaxy populations hosting a radio-excess AGN. Here we use the combined All Galaxies Sample (see Section 2 and Fig. 1) and combined Radio-excess AGN Sample (see Section 4 and Fig. 1) in the GOODS-N and COSMOS/UltraVISTA fields. The All Galaxies Sample and the host galaxies of the Radio-excess AGN Sample had been divided into SFGs and QGs according to the UVJ selection method (see Section 3.4). In Sections 6.1 and 6.2, we use the observational data to calculate the probability of a SFG or a QG with the stellar mass M_\star and at redshift z hosting a radio-excess AGN with the 1.4 GHz luminosity L_R in each redshift bin. In Section 6.3, we use the method of Aird et al. (2012) to quantitatively calculate the probability of a SFG or a QG hosting a radio-excess AGN as a function of stellar mass, radio luminosity, and redshift. This method is based on the maximum-likelihood approach, which does not require data binning for stellar mass, luminosity, and redshift (Aird et al. 2012). Here we do not consider the star-formation contamination for the AGN radio luminosity, while for most of our Radio-excess

AGN Sample, contribution from star-formation to the radio luminosity have been verified to be not significant compared to that from AGN.

6.1. Calculate the probability for observational data

In order to conveniently compare the data and the best-fit model, we divided our All Galaxies Sample and Radio-excess AGN Sample into 6 redshift bins (same as the redshift bins in Section 4). Within each redshift bin, we subdivided our All Galaxies Sample and Radio-excess AGN Sample into different stellar mass bins. The conditional probability density function $p(L_R | M_\star, z)$ describes the probability of a galaxy with stellar mass M_\star and at redshift z hosting a radio-excess AGN with 1.4 GHz luminosity L_R . Following Aird et al. (2012), here $p(L_R | M_\star, z)$ is defined as the probability density per logarithmic luminosity interval (units are dex⁻¹). Thus, $p(L_R | M_\star, z)$ can be converted to AGN fraction (f_{AGN}) according to

$$f_{\text{AGN}}(M_\star, z) = \int_{\log L_{\text{lim}}}^{\infty} p(L_R | M_\star, z) d \log L_R. \quad (20)$$

Here f_{AGN} is defined as the fraction of galaxies with stellar mass M_\star and at redshift z that host a radio-excess AGN, L_{lim} is the lower limit of the radio luminosity. For the combined observational data from the GOODS-N and COSMOS/UltraVISTA fields, in each redshift bin, $p(L_R | M_\star, z)$ in the m th stellar mass bin and the n th luminosity bin is defined by

$$p(L_n | M_m, z) = \frac{N_{\text{AGN},mn}}{N_{\text{gal},m} \Delta \log L_n} = \frac{f_{\text{AGN}}(M_\star, z)}{\Delta \log L_n}, \quad (21)$$

where $N_{\text{AGN},mn}$ is the number of the Radio-excess AGN Sample in the m th stellar mass bin and the n th luminosity bin, $N_{\text{gal},m}$ is the number of the All Galaxies Sample in the m th stellar mass bin, and $\Delta \log L_n$ is the width of the n th luminosity bin. It is worth stating that when calculating the probability of SFGs (or QGs, or all galaxies) hosting a radio-excess AGN, here $N_{\text{AGN},mn}$ refers to all the radio-excess AGNs hosted by SFGs (or QGs, or all galaxies) and N_{gal} refers to all the SFGs (or QGs,

or all galaxies) in the All Galaxies Sample. The estimates of $p(L_R | M_\star, z)$ for SFGs in 6 redshift bins are shown as colored symbols in Fig. F.1 and Fig. F.2. The radio-excess AGNs in both QGs and all galaxies exhibit similar trends to SFGs, so we do not show their details here. The probability of a galaxy hosting a radio-excess AGN with a given L_R increases with M_\star at all redshift bins (see Fig. F.1), which is consistent with the previous works (e.g., Best et al. 2005; Sabater et al. 2019). The probability of a galaxy with a given M_\star hosting a radio-excess AGN decreases with L_R , which is also consistent with previous works (e.g., Best et al. 2005). These trends of radio-excess AGNs in this work are consistent with those of X-ray AGNs (e.g., Haggard et al. 2010; Aird et al. 2012; Wang et al. 2017).

6.2. Simple χ^2 fits in each redshift bin

To quantitatively study the trends of $p(L_R | M_\star, z)$, we apply χ^2 fits to the results calculated by Equation 21 (see the data points in Fig. F.1 and Fig. F.2). Next we take the analysis for SFGs as an example to show the detailed analysis procedures. At each fixed L_R , we assume a simple power-law relation for $p(L_R | M_\star, z)$ as a function of M_\star ,

$$\log[p(L_R | M_\star, z)] = a + b \log \left[\frac{M_\star}{10^{11} M_\odot} \right], \quad (22)$$

where a and b are the intercept and slope of the relation, respectively. The best-fit values for a and b in each L_R bin and each redshift bin are presented in the right column of Fig. F.1. The averaged best-fit reduced- χ^2 over all the redshift bins and all the L_R bins is 1.22. In all redshift bins, the intercept a decreases with larger L_R , while the slope b does not show significant changes. Similarly, for each fixed M_\star , $p(L_R | M_\star, z)$ as a function of L_R can be defined as

$$\log[p(L_R | M_\star, z)] = c + d \log \left[\frac{L_R}{10^{23} \text{ W Hz}^{-1}} \right], \quad (23)$$

where c and d are the intercept and slope of the relation, respectively. The best-fit parameters in each M_\star bin and each redshift bin are shown in the right column of Fig. F.2. The averaged best-fit reduced- χ^2 over all the redshift bins and all the M_\star bins is 1.76. In all redshift bins, the intercept c decreases with higher M_\star , while the slope d nearly keeps constant. These results indicate that the slope b (or the slope d) of $p(L_R | M_\star, z)$ as a function of M_\star (or L_R) is independent of L_R (or M_\star). QGs and all galaxies show similar trends but different best-fit parameters comparing to SFGs. Given that we mainly focus on the trends in this section, for brevity, we do not discuss their results in details here. The main differences among different galaxy populations are discussed in Section 6.3.4 and shown in Fig. 7.

6.3. Redshift evolution

The above analysis starts by dividing sources into different redshift bins, then binning the sources according to their M_\star and L_R within each redshift bin, and finally fitting the binned data. Therefore, the best-fit result may be significantly affected by the bin size of redshift, M_\star , and L_R , and the information of each individual galaxy cannot be fully utilized due to the binning. Therefore, next we utilize the maximum likelihood fitting approach in Aird et al. (2012) to measure the dependence of $p(L_R | M_\star, z)$ on both M_\star and L_R . At first, in Section 6.3.1, we introduce the fitting approach applied to our samples. Then we test this approach in each redshift bin in Section 6.3.2. Finally, in

Section 6.3.3, we apply this approach incorporating the redshift evolution in order to remove the effects brought by the redshift binning.

6.3.1. Maximum-likelihood fitting

According to the results in Section 6.2, the slope b (or d) in Equation 22 (or 23) of $p(L_R | M_\star, z)$ as a function of M_\star (or L_R) is independent of L_R (or M_\star). It means that $p(L_R | M_\star, z)$ at a fixed redshift can be expressed as a separable function of M_\star and L_R in the form of

$$p(L_R | M_\star, z) d \log L_R = K \left(\frac{M_\star}{M_0} \right)^{\gamma_M} \left(\frac{L_R}{L_0} \right)^{\gamma_L} d \log L_R, \quad (24)$$

where the scaling factor M_0 is set to $10^{11} M_\odot$, the scaling factor L_0 is set to $10^{23} \text{ W Hz}^{-1}$, K is the normalization, γ_M and γ_L are indices. The best-fit parameters are found through maximizing the log-likelihood function,

$$\ln \mathcal{L} = -\mathcal{N} + \sum_{k=1}^{N_i^{\text{AGN}}} \ln p_k, \quad (25)$$

where N_i^{AGN} is the number of radio-excess AGNs in the GOODS-N and COSMOS/UltraVISTA fields in the i th redshift bin, p_k is the probability of a galaxy with stellar mass M_k hosting a radio-excess AGN with 1.4 GHz luminosity L_k :

$$p_k = p(L_k | M_k, z_k) = K \left(\frac{M_k}{M_0} \right)^{\gamma_M} \left(\frac{L_k}{L_0} \right)^{\gamma_L}. \quad (26)$$

The expected number of radio-excess AGNs, \mathcal{N} , is defined as

$$\begin{aligned} \mathcal{N} &= \sum_{j=1}^{N_i^{\text{gal,gn}}} \int_{\log L_{\text{lim,gn},j}}^{\infty} p(L_R | M_j, z_j) d \log L_R \\ &+ \sum_{j=1}^{N_i^{\text{gal,cs}}} \int_{\log L_{\text{lim,cs},j}}^{\infty} p(L_R | M_j, z_j) d \log L_R \\ &= \sum_{j=1}^{N_i^{\text{gal,gn}}} K \left(\frac{M_j}{M_0} \right)^{\gamma_M} \int_{\log L_{\text{lim,gn},j}}^{\infty} \left(\frac{L_R}{L_0} \right)^{\gamma_L} d \log L_R, \\ &+ \sum_{j=1}^{N_i^{\text{gal,cs}}} K \left(\frac{M_j}{M_0} \right)^{\gamma_M} \int_{\log L_{\text{lim,cs},j}}^{\infty} \left(\frac{L_R}{L_0} \right)^{\gamma_L} d \log L_R, \end{aligned} \quad (27)$$

where $N_i^{\text{gal,gn}}$ and $N_i^{\text{gal,cs}}$ are the numbers of galaxies in the i th redshift bin for the GOODS-N and COSMOS/UltraVISTA fields, respectively. L_{lim} of the GOODS-N field ($L_{\text{lim,gn},j}$) corresponds to the 5σ detection limit of the radio survey at redshift z_j (see Fig. 2), while for the COSMOS ($L_{\text{lim,cs},j}$) field, it corresponds to the $L_{1.4\text{GHz}}$ threshold for correcting the AGN classification purity (see details in Appendix B). The 1σ error of each model parameter is estimated by the maximum projection of $\Delta S = 1.0$ where $S = -2 \ln \mathcal{L}$ according to Aird et al. (2012).

6.3.2. Results in each redshift bin

In each redshift bin, we use the above maximum-likelihood fitting approach to constrain $p(L_R | M_\star, z)$ for SFGs, QGs, and all galaxies. The best-fit values for γ_M , γ_L , and K in each redshift bin are shown in the form of colored symbols in Fig. 7. For both

SFGs and QGs, we find that γ_M and γ_L almost keep constant at all redshift bins except at $z \lesssim 0.5$ (see detailed discussions in Section 6.3.3). For all galaxies, γ_M and γ_L do not show any significant changes with redshift ($0.1 < z \leq 4.0$), which is consistent with the trends of X-ray AGNs in Aird et al. (2012) at $0.2 < z \leq 1.0$. For SFGs, QGs and all galaxies, the normalization K significantly increases with redshift. In addition, SFGs and QGs show significantly different γ_M , γ_L , and K , which will be discussed in details in Section 6.3.4. Overall, the probability of a galaxy with a given stellar mass hosting a radio-excess AGN with a given radio luminosity increases towards higher redshift. This indicates higher AGN activities and potentially more significant AGN feedbacks towards higher redshift.

6.3.3. Incorporating redshift evolution into the maximum-likelihood fitting

According to the results of Section 6.3.2, both γ_M and γ_L are nearly constant over the entire redshift range, which indicates that the redshift evolution of $p(L_R | M_\star, z)$ can be assumed to be independent of L_R and M_\star . Only the normalization K shows an evident evolution with redshift, so $p(L_R | M_\star, z)$ incorporating the redshift evolution for K with a simple power-law can be rewritten as

$$p(L_R | M_\star, z) d \log L_R = A \left(\frac{1+z}{1+z_0} \right)^{\gamma_z} \left(\frac{M_\star}{M_0} \right)^{\gamma_M} \left(\frac{L_R}{L_0} \right)^{\gamma_L} d \log L_R, \quad (28)$$

where the scaling factor z_0 is set to be 2.0 (median of the redshift range for our sample), A is the overall normalization. Thus,

$$K = A \left(\frac{1+z}{1+z_0} \right)^{\gamma_z}. \quad (29)$$

Then we modify $p(L_R | M_\star, z)$ in Equations 25–27 with Equation 28 to perform maximum-likelihood fitting over the entire redshift range ($0.1 < z \leq 4.0$). The best-fit parameters are listed in Table 2 and plotted in Fig. 7 as the colored lines. The redshift evolution model over the entire redshift range is almost consistent with the result obtained in each redshift bin (colored symbols in Fig. 7).

To compare the model with the observational data, we use the $N_{\text{obs}}/N_{\text{mdl}}$ method of Aird et al. (2012) (see Equation 14 in their paper) to scale the observed radio-excess AGN number (N_{obs}) by the expected number estimated by the model (N_{mdl}) in each redshift bin (see Equation 28). Overall, the binned estimates for the observational data in each redshift bin are well described by the best-fit model obtained with maximum-likelihood fitting over the entire redshift range (see results for SFGs in Fig. 8, for QGs in Fig. G.1, for all galaxies in Fig. G.2). However, the best-fit model cannot fully explain the data in the following cases: low-luminosity radio-excess AGN in SFGs at $0.1 < z \leq 1.0$ ($L_{1.4\text{GHz}} < 10^{23} \text{ W Hz}^{-1}$; see Panel A1 in Fig. 8) and at $2 < z \leq 4$ ($L_{1.4\text{GHz}} < 10^{23.5} \text{ W Hz}^{-1}$; see Panel D1 in Fig. 8), radio-excess AGN in massive SFGs ($M_\star > 10^{11.5} M_\odot$) at $0.1 < z \leq 1.0$ (see Panels A2 in Fig. 8), radio-excess AGN in low-mass QGs ($M_\star < 10^{10} M_\odot$) at $0.1 < z \leq 1.0$ (see Panels A2 in Fig. G.1, respectively). The following reasons might explain the slight differences between observational data and model predictions. In the analysis, we assume that γ_M (or γ_L) is independent of L_R (or M_\star) and redshift (see Sections 6.2 and 6.3.2). On the one hand, a mild dependence of γ_M (or γ_L) on L_R (or M_\star) cannot be fully ruled out. In addition, γ_M may be different between low-mass

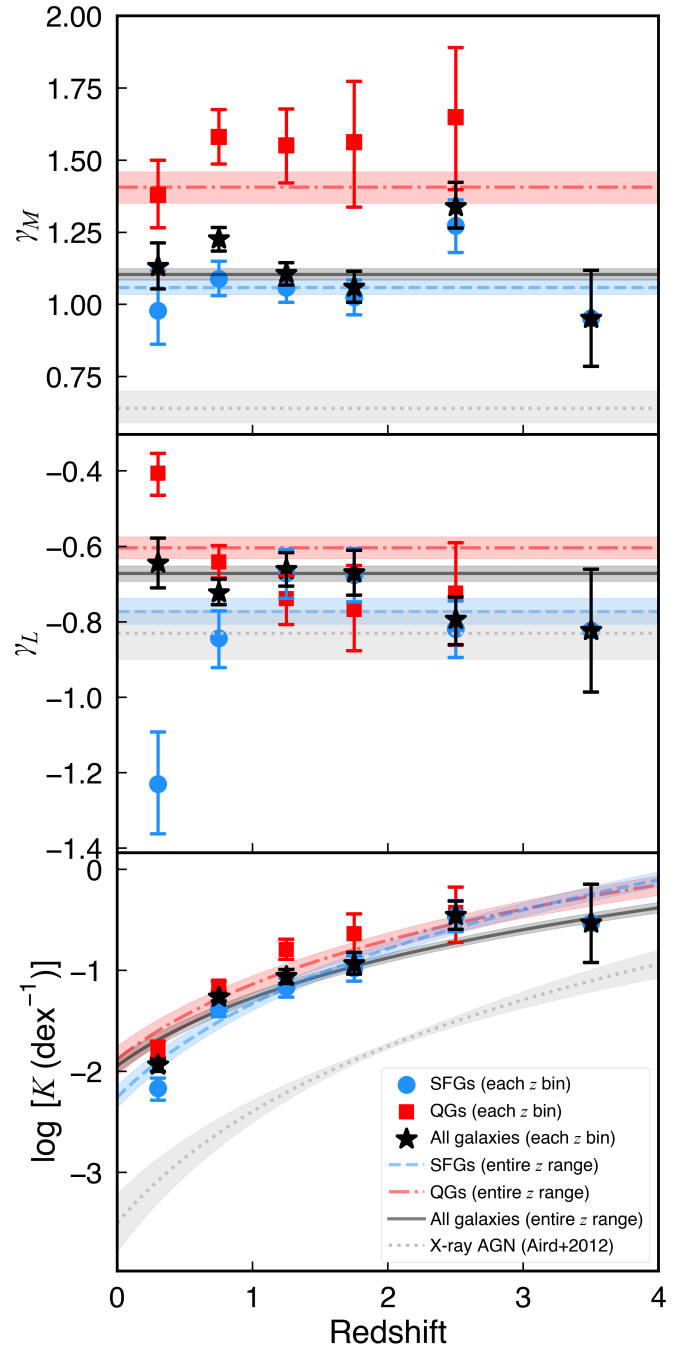


Fig. 7: Best-fit parameters of the maximum-likelihood fitting for $p(L_R | M_\star, z)$ of SFGs (blue circles and blue dashed lines), QGs (red squares and red dash-dotted lines), and all galaxies (black stars and black solid lines). Colored symbols represent the best-fit parameters obtained by Equations 24–27 in each redshift bin (see details in Sections 6.3.1 and 6.3.2). The colored lines show the best-fit results over the entire redshift range obtained by Equations 28–29 and 25–27 (see details in Section 6.3.3). The dotted gray lines represent the results for the X-ray AGNs in Aird et al. (2012)

and high-mass galaxies (Williams & Röttgering 2015; Zhu et al. 2023), while γ_L may also change from low-luminosity to high-luminosity populations (Best et al. 2005). On the other hand, a weak evolution of both γ_M and γ_L with redshift might exist (see

Table 2: Best-fit parameters from Maximum-likelihood Fitting with redshift evolution.

Type	log A	γ_M	γ_L	γ_z
SFG	-0.79 ± 0.07	1.06 ± 0.03	-0.77 ± 0.03	3.08 ± 0.20
QG	-0.70 ± 0.08	1.41 ± 0.05	-0.60 ± 0.03	2.47 ± 0.28
All	-0.88 ± 0.05	1.10 ± 0.02	-0.67 ± 0.02	2.24 ± 0.14

colored symbols in Fig. 7 and discussion in Section 7). Some works had found that γ_M decreases from the local universe to $z \sim 2$ (Williams & Röttgering 2015; Zhu et al. 2023), while Kondapally et al. (2022) found a weak positive evolution with redshift (for SFGs only). Even so, on the whole our model can still well describe the redshift evolution of radio-excess AGN fraction across the entire redshift range.

6.3.4. Quantitative relation of radio-excess AGN fraction in SFGs and QGs

To sum up, we obtain quantitative relations for the probability of SFGs, QGs, or all galaxies hosting a radio-excess AGN as a function of M_\star , L_R , and redshift, respectively:

$$\begin{aligned}
 p(L_R | M_\star, z)_{\text{SFG}} &= 10^{-0.79} \left(\frac{M_\star}{M_0} \right)^{1.06} \left(\frac{L_R}{L_0} \right)^{-0.77} \left(\frac{1+z}{1+z_0} \right)^{3.08}, \\
 p(L_R | M_\star, z)_{\text{QG}} &= 10^{-0.70} \left(\frac{M_\star}{M_0} \right)^{1.41} \left(\frac{L_R}{L_0} \right)^{-0.60} \left(\frac{1+z}{1+z_0} \right)^{2.47}, \\
 p(L_R | M_\star, z)_{\text{All}} &= 10^{-0.88} \left(\frac{M_\star}{M_0} \right)^{1.10} \left(\frac{L_R}{L_0} \right)^{-0.67} \left(\frac{1+z}{1+z_0} \right)^{2.24},
 \end{aligned} \tag{30}$$

where M_0 is set to $10^{11} M_\odot$, L_0 is set to $10^{23} \text{ W Hz}^{-1}$, and z_0 is set to 2.0. These best-fit parameters and their uncertainties are summarized in Table 2. SFGs and QGs have significantly different evolution trends for radio-excess AGN fraction (also see Fig. 7). QGs have larger γ_M and γ_L than SFGs, which indicates that radio-excess AGNs in QGs prefer to reside in more massive galaxies with higher radio luminosity compared to those in SFGs. Both SFGs and QGs have an increasing radio-excess AGN fraction with redshift (see Fig. 7). SFGs show a larger γ_z than QGs (see Table 2), which implies that radio-excess AGN fractions in SFGs increase more rapidly towards higher redshift than those in QGs.

7. Discussion: comparison with previous works

As Equation 30 shows, we obtain a smaller γ_M (~ 1) than that in Best et al. (2005) ($\gamma_M \sim 2.5$; $0.03 < z < 0.3$). Our result is consistent with that in Williams & Röttgering (2015) at $1.5 < z < 2$ ($\gamma_M \sim 1.0$), while their results showed a decreasing γ_M trend from the local universe ($\gamma_M \sim 2.7$) to $z \sim 2$. Zhu et al. (2023) also found a decreasing stellar-mass dependence from $z \sim 0.3$ to $z \sim 2.3$. In addition, the dependence of radio-AGN fraction on the stellar mass may change when $M_\star > 10^{11} M_\odot$ (Williams & Röttgering 2015; Zhu et al. 2023). The differences between our and their results may be due to the different radio-AGN selections and different calculation methods. Previous works usually focused on powerful radio-AGNs ($L_{1.4\text{GHz}} > 10^{23}$ or $10^{24} \text{ W Hz}^{-1}$), while our sample additionally includes some faint radio-AGNs with $L_{1.4\text{GHz}} < 10^{23} \text{ W Hz}^{-1}$.

Moreover, the different evolution trends of radio-AGN in SFGs and QGs indicate that disregarding the galaxy types may have a non-negligible effect on statistical results. Kondapally et al. (2022) proposed for the first time a radio-AGNs study for QGs and SFGs separately. They found that low-excitation radio galaxies in QGs have a larger γ_M (~ 2.5) than those in SFGs ($\gamma_M \sim 1.37$). We found a similar trend but lower γ_M values than their results ($\gamma_M \sim 1.4$ for QGs and $\gamma_M \sim 1.0$ for SFGs in our work). One possible reason for this difference may be that we focus on different radio-AGNs samples comparing to Kondapally et al. (2022) (see details in Section 5.3). Our results show that γ_M has no significant evolution with redshift at $0.1 < z \leq 4.0$, while for LERGs in Kondapally et al. (2022) at $0.3 < z \leq 1.5$, γ_M shows no significant evolution for QGs and a positive evolution for SFGs.

Given that we use the same calculation method as Aird et al. (2012) (see details in Section 6.3), we also compare the results for radio-excess AGNs with those for X-ray AGNs from Aird et al. (2012) which are plotted as gray dotted lines in Fig. 7. Comparing to X-ray AGNs (Aird et al. 2012), evolutions of radio-excess AGN fraction (see black solid lines in Fig. 7) have a larger γ_M , which indicates that radio-excess AGNs tend to reside in more massive galaxies (see Fig. 7). X-ray AGN fractions in red sequence galaxies exhibit a more rapid redshift evolution than those in blue cloud galaxies (Aird et al. 2012; Wang et al. 2017), while radio-excess AGNs fraction in SFGs increases more rapidly towards higher redshift than those in QGs. These different evolution trends between radio-excess AGNs and X-ray AGNs suggest that black holes with different accretion states may influence their host galaxies in different modes.

In addition, we also examine whether M_\star -dependent IRRC (Delvecchio et al. 2021) affects the results about the probability of hosting a radio-excess AGN. Following van der Vlugt et al. (2022), we select radio-excess AGNs with q_{TIR} deviating more than 3σ from the M_\star -dependent IRRC of Delvecchio et al. (2021). Then we recalculate the probability of a radio-excess AGN hosted by SFGs using Equation 28 (see the dark blue region in Fig. H.1) which is consistent with the results based on the radio-excess-AGN selection method in Section 4 (see the green region in Fig. H.1). This result indicates that using the M_\star -dependent IRRC (Delvecchio et al. 2021) does not alter the results in this work.

8. Summary

Firstly we use the optical to MIR surveys to select a All Galaxies Sample with $\sim 400,000$ sources at $0.1 < z < 4$ in GOODS-N and COSMOS/UltraVISTA fields (totaling 1.6 degree^2 ; Section 2). After cross-matching with the deep/large radio surveys (1.4 GHz or 3 GHz) in these fields, we select 7494 radio sources with S/N of radio flux ≥ 5 at $0.1 < z < 4$ as our Radio Sources Sample (Section 2). Combining with the deblended IR photometry in these fields, we calculate the infrared-radio ratio (q_{TIR}) distributions of these radio sources to select a Radio-excess AGN Sample with 983 sources (Section 4.1). Next we subdivide all our samples into SFGs and QGs using the UVJ method. Based on the Radio Sources Sample, we construct 1.4 GHz radio luminosity functions (RLFs) for SFGs and radio-excess AGNs at $0.1 < z < 4$ (Section 5.1), respectively, and study their evolutions with redshift. Based on the All Galaxies Sample and Radio-excess AGN Sample, we further investigate the probability of different galaxies populations (SFGs and QGs) hosting a radio-excess AGN as a function of

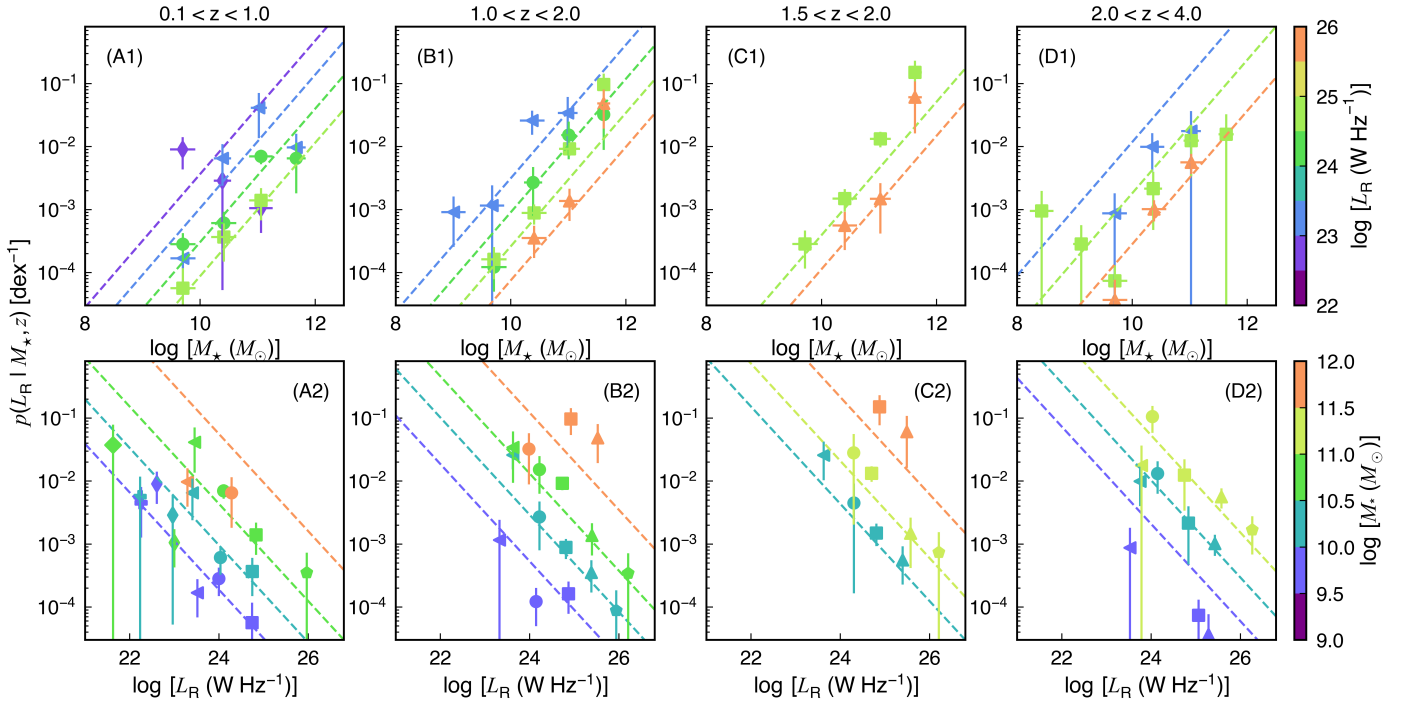


Fig. 8: Estimates of $p(L_R | M_*, z)$ as a function of M_* and L_R based on our maximum-likelihood fitting results for SFGs. Colored dashed lines in both top and bottom rows represent our best-fit model from the unbinned maximum-likelihood fitting (see Equation 28 and Table 2) through combining data in the GOODS-N and COSMOS/UltraVISTA fields over the entire redshift range ($0.1 < z < 4$) evaluated at the center of each redshift bin. Binned data points are scaled with the probability estimated by the model (see Equation 28) using the $N_{\text{obs}}/N_{\text{mdl}}$ method of Aird et al. (2012) (see details in Section 6.3.3). In the top panel, different colors represent different M_* bins. In the bottom panel, different colors show different L_R bins.

stellar mass, radio luminosity, and redshift. The main conclusions we have obtained are shown as follows.

1. The q_{TIR} value of SFGs shows a weak evolution with redshift: $\bar{q}_{\text{TIR}} = 2.62 \times (1+z)^{-0.08}$ (Section 4.2), which is generally consistent with previous works.
2. The evolution of RLFs with redshift for SFGs can be well described by the pure luminosity evolution model of $L_* \propto (1+z)^{-0.34 \times z + 3.57}$ (Section 5.2). The evolution of AGN RLFs follows the pure density evolution model of $\Phi_* \propto (1+z)^{-0.77 \times z + 2.69}$ (Section 5.3).
3. The evolution of crossover luminosity between SFG RLFs and AGN RLFs is shown as $L_D = 10^{22.9} \times (1+z)^{0.06 \times z + 3.05} \text{ W Hz}^{-1}$, which can be used to select powerful radio AGNs at different redshifts through solely radio surveys (Section 5.4). This result also indicate a decreasing contribution of AGNs to entire radio populations towards higher redshift.
4. The probability of a galaxy hosting a radio-excess AGN is shown as a function of stellar mass, radio luminosity, and redshift: $p(L_R | M_*, z) = 10^{-0.79} \left(\frac{M_*}{M_0}\right)^{1.06} \left(\frac{L_R}{L_0}\right)^{-0.77} \left(\frac{1+z}{1+z_0}\right)^{3.08}$ for SFGs, $p(L_R | M_*, z) = 10^{-0.70} \left(\frac{M_*}{M_0}\right)^{1.41} \left(\frac{L_R}{L_0}\right)^{-0.60} \left(\frac{1+z}{1+z_0}\right)^{2.47}$ for QGs (Section 6.3). It indicates that radio-excess AGNs in QGs prefer to reside in more massive galaxies with larger radio luminosity than those in SFGs. The fractions of radio-excess AGNs in both SFGs and QGs are increasing from the local universe to the higher redshift. In addition, this increasing trend in SFGs is more significant than in QGs.

The above studies can lay the foundation for further investigation with the upcoming revolutionary radio facilities, such

as Square Kilometer Array (SKA; Dewdney et al. 2009; Norris et al. 2013; McAlpine et al. 2015) and the Next Generation Very Large Array (ngVLA; Hughes et al. 2015).

Acknowledgements. We thank the referee for constructive comments that greatly improved this paper. This work is supported by the National Natural Science Foundation of China (Project No. 12173017 and Key Project No. 12141301).

References

- Aird, J., Coil, A. L., Moustakas, J., et al. 2012, *ApJ*, 746, 90
Aird, J., Nandra, K., Laird, E. S., et al. 2010, *MNRAS*, 401, 2531
Alberts, S., Rujopakarn, W., Rieke, G. H., Jagannathan, P., & Nyland, K. 2020, *ApJ*, 901, 168
An, F., Vaccari, M., Smail, I., et al. 2021, *MNRAS*, 507, 2643
Appleton, P. N., Fadda, D. T., Marleau, F. R., et al. 2004, *ApJS*, 154, 147
Arnouts, S., Moscardini, L., Vanzella, E., et al. 2002, *MNRAS*, 329, 355
Baldwin, J. A., Phillips, M. M., & Terlevich, R. 1981, *PASP*, 93, 5
Barbieri, L. G. C., Snios, B., Sobolewska, M., Siemiginowska, A., & Schwartz, D. A. 2022, *MNRAS*, 513, 4673
Barro, G., Pérez-González, P. G., Cava, A., et al. 2019, *ApJS*, 243, 22
Bell, E. F. 2003, *ApJ*, 586, 794
Best, P. N., Kauffmann, G., Heckman, T. M., et al. 2005, *MNRAS*, 362, 25
Best, P. N., Kondapally, R., Williams, W. L., et al. 2023, *MNRAS*, 523, 1729
Bonchi, A., La Franca, F., Melini, G., Bongiorno, A., & Fiore, F. 2013, *MNRAS*, 429, 1970
Boquien, M., Burgarella, D., Roehlly, Y., et al. 2019, *A&A*, 622, A103
Brammer, G. B., van Dokkum, P. G., & Coppi, P. 2008, *ApJ*, 686, 1503
Brown, M. J. I., Jannuzi, B. T., Floyd, D. J. E., & Mould, J. R. 2011, *ApJ*, 731, L41
Bruzual, G. & Charlot, S. 2003, *MNRAS*, 344, 1000
Burgarella, D., Buat, V., & Iglesias-Páramo, J. 2005, *MNRAS*, 360, 1413
Calistro Rivera, G., Williams, W. L., Hardcastle, M. J., et al. 2017, *MNRAS*, 469, 3468
Calzetti, D., Armus, L., Bohlin, R. C., et al. 2000, *ApJ*, 533, 682
Cera, L., Smolčić, V., Delvecchio, I., et al. 2018, *A&A*, 620, A192

- Chabrier, G. 2003, *ApJ*, 586, L133
- Cochrane, R. K., Kondapally, R., Best, P. N., et al. 2023, *MNRAS*, 523, 6082
- Condon, J. J. 1992, *ARA&A*, 30, 575
- Condon, J. J. & Dressel, L. L. 1978, *ApJ*, 221, 456
- Condon, J. J., Matthews, A. M., & Broderick, J. J. 2019, *ApJ*, 872, 148
- Dale, D. A., Helou, G., Magdis, G. E., et al. 2014, *ApJ*, 784, 83
- Davé, R., Anglés-Alcázar, D., Narayanan, D., et al. 2019, *MNRAS*, 486, 2827
- Del Moro, A., Alexander, D. M., Mullaney, J. R., et al. 2013, *A&A*, 549, A59
- Delhaize, J., Smolčić, V., Delvecchio, I., et al. 2017, *A&A*, 602, A4
- Delvecchio, I., Daddi, E., Sargent, M. T., et al. 2022, *A&A*, 668, A81
- Delvecchio, I., Daddi, E., Sargent, M. T., et al. 2021, *A&A*, 647, A123
- Delvecchio, I., Smolčić, V., Zamorani, G., et al. 2017, *A&A*, 602, A3
- Dewdney, P. E., Hall, P. J., Schilizzi, R. T., & Lazio, T. J. L. W. 2009, *IEEE Proceedings*, 97, 1482
- Donley, J. L., Koekemoer, A. M., Brusa, M., et al. 2012, *ApJ*, 748, 142
- Donley, J. L., Rieke, G. H., Rigby, J. R., & Pérez-González, P. G. 2005, *ApJ*, 634, 169
- Donoso, E., Best, P. N., & Kauffmann, G. 2009, *MNRAS*, 392, 617
- Donoso, E., Li, C., Kauffmann, G., Best, P. N., & Heckman, T. M. 2010, *MNRAS*, 407, 1078
- Draine, B. T. & Li, A. 2007, *ApJ*, 657, 810
- Dubner, G. & Giacani, E. 2015, *A&A Rev.*, 23, 3
- Dullo, B. T., Knapen, J. H., Beswick, R. J., et al. 2023, *MNRAS*, 522, 3412
- Enia, A., Talia, M., Pozzi, F., et al. 2022, *ApJ*, 927, 204
- Fabian, A. C. 2012, *ARA&A*, 50, 455
- Fiore, F., Feruglio, C., Shankar, F., et al. 2017, *A&A*, 601, A143
- Foreman-Mackey, D., Hogg, D. W., Lang, D., & Goodman, J. 2013, *PASP*, 125, 306
- Franzen, T. M. O., Seymour, N., Sadler, E. M., et al. 2021, *PASA*, 38, e041
- Gim, H. B., Yun, M. S., Owen, F. N., et al. 2019, *ApJ*, 875, 80
- Grogan, N. A., Kocevski, D. D., Faber, S. M., et al. 2011, *ApJS*, 197, 35
- Grupponi, C., Pozzi, F., Rodighiero, G., et al. 2013, *MNRAS*, 432, 23
- Haggard, D., Green, P. J., Anderson, S. F., et al. 2010, *ApJ*, 723, 1447
- Hardcastle, M. J. & Croston, J. H. 2020, *New A Rev.*, 88, 101539
- Helou, G., Soifer, B. T., & Rowan-Robinson, M. 1985, *ApJ*, 298, L7
- Ho, L. C. 2008, *ARA&A*, 46, 475
- Hughes, A. M., Beasley, A., & Carilli, C. 2015, in *IAU General Assembly*, Vol. 29, 2255106
- Ilbert, O., Arnouts, S., McCracken, H. J., et al. 2006, *A&A*, 457, 841
- Iverson, R. J., Magnelli, B., Ibar, E., et al. 2010, *A&A*, 518, L31
- Janssen, R. M. J., Röttgering, H. J. A., Best, P. N., & Brinchmann, J. 2012, *A&A*, 541, A62
- Jarvis, M., Taylor, R., Agudo, I., et al. 2016, in *MeerKAT Science: On the Pathway to the SKA*, 6
- Jin, S., Daddi, E., Liu, D., et al. 2018, *ApJ*, 864, 56
- Kauffmann, G. & Heckman, T. M. 2009, *MNRAS*, 397, 135
- Kauffmann, G., Heckman, T. M., Tremonti, C., et al. 2003, *MNRAS*, 346, 1055
- Kewley, L. J., Maier, C., Yabe, K., et al. 2013, *ApJ*, 774, L10
- Koekemoer, A. M., Faber, S. M., Ferguson, H. C., et al. 2011, *ApJS*, 197, 36
- Kolwa, S., Jarvis, M. J., McAlpine, K., & Heywood, I. 2019, *MNRAS*, 482, 5156
- Kondapally, R., Best, P. N., Cochrane, R. K., et al. 2022, *MNRAS*, 513, 3742
- Kondapally, R., Best, P. N., Raouf, M., et al. 2023, *MNRAS*, 523, 5292
- Kriek, M., van Dokkum, P. G., Labbé, I., et al. 2009, *ApJ*, 700, 221
- Kukreti, P., Morganti, R., Tadhunter, C., & Santoro, F. 2023, *arXiv e-prints*, arXiv:2305.03725
- Lacy, M., Storie-Lombardi, L. J., Sajina, A., et al. 2004, *ApJS*, 154, 166
- Liu, D., Daddi, E., Dickinson, M., et al. 2018, *ApJ*, 853, 172
- Luo, B., Brandt, W. N., Xue, Y. Q., et al. 2017, *ApJS*, 228, 2
- Magliocchetti, M. 2022, *A&A Rev.*, 30, 6
- Magliocchetti, M., Maddox, S. J., Hawkins, E., et al. 2004, *MNRAS*, 350, 1485
- Magliocchetti, M., Popesso, P., Brusa, M., et al. 2017, *MNRAS*, 464, 3271
- Magnelli, B., Ivison, R. J., Lutz, D., et al. 2015, *A&A*, 573, A45
- Malavasi, N., Bardelli, S., Ciliegi, P., et al. 2015, *A&A*, 576, A101
- Matthews, A. M., Condon, J. J., Cotton, W. D., & Mauch, T. 2021, *ApJ*, 914, 126
- Matzeu, G. A., Brusa, M., Lanzuisi, G., et al. 2023, *A&A*, 670, A182
- Mauch, T. & Sadler, E. M. 2007, *MNRAS*, 375, 931
- McAlpine, K., Jarvis, M. J., & Bonfield, D. G. 2013, *MNRAS*, 436, 1084
- McAlpine, K., Prandoni, I., Jarvis, M., et al. 2015, in *Advancing Astrophysics with the Square Kilometre Array (AASKA14)*, 83
- Merloni, A., Heinz, S., & di Matteo, T. 2003, *MNRAS*, 345, 1057
- Molnár, D. C., Sargent, M. T., Leslie, S., et al. 2021, *MNRAS*, 504, 118
- Morrison, G. E., Owen, F. N., Dickinson, M., Ivison, R. J., & Ibar, E. 2010, *ApJS*, 188, 178
- Mullaney, J. R., Alexander, D. M., Goulding, A. D., & Hickox, R. C. 2011, *MNRAS*, 414, 1082
- Ni, Q., Aird, J., Merloni, A., et al. 2023, *MNRAS[arXiv:2307.00051]*
- Noll, S., Burgarella, D., Giovannoli, E., et al. 2009, *A&A*, 507, 1793
- Norris, R. P., Afonso, J., Bacon, D., et al. 2013, *PASA*, 30, e020
- Novak, M., Smolčić, V., Delhaize, J., et al. 2017, *A&A*, 602, A5
- Novak, M., Smolčić, V., Schinnerer, E., et al. 2018, *A&A*, 614, A47
- Ocran, E. F., Taylor, A. R., Vaccari, M., et al. 2020, *MNRAS*, 491, 5911
- Owen, F. N. 2018, *ApJS*, 235, 34
- Panessa, F., Baldi, R. D., Laor, A., et al. 2019, *Nature Astronomy*, 3, 387
- Park, S. Q., Barmby, P., Fazio, G. G., et al. 2008, *ApJ*, 678, 744
- Pasini, T., Brüggen, M., Hoang, D. N., et al. 2022, *A&A*, 661, A13
- Peacock, J. A. & Nicholson, D. 1991, *MNRAS*, 253, 307
- Pérez-González, P. G., Rieke, G. H., Egami, E., et al. 2005, *ApJ*, 630, 82
- Pérez-González, P. G., Rieke, G. H., Villar, V., et al. 2008, *ApJ*, 675, 234
- Pillepich, A., Springel, V., Nelson, D., et al. 2018, *MNRAS*, 473, 4077
- Popesso, P., Concas, A., Cresci, G., et al. 2023, *MNRAS*, 519, 1526
- Radcliffe, J. F., Barthel, P. D., Thomson, A. P., et al. 2021, *A&A*, 649, A27
- Sabater, J., Best, P. N., Hardcastle, M. J., et al. 2019, *A&A*, 622, A17
- Sabater, J., Best, P. N., Tasse, C., et al. 2021, *A&A*, 648, A2
- Sargent, M. T., Schinnerer, E., Murphy, E., et al. 2010a, *ApJS*, 186, 341
- Sargent, M. T., Schinnerer, E., Murphy, E., et al. 2010b, *ApJ*, 714, L190
- Saunders, W., Rowan-Robinson, M., Lawrence, A., et al. 1990, *MNRAS*, 242, 318
- Schmidt, M. 1968, *ApJ*, 151, 393
- Schreiber, C., Pannella, M., Elbaz, D., et al. 2015, *A&A*, 575, A74
- Scoville, N., Aussel, H., Brusa, M., et al. 2007, *ApJS*, 172, 1
- Seymour, N., Dwelly, T., Moss, D., et al. 2008, *MNRAS*, 386, 1695
- Smolčić, V., Delvecchio, I., Zamorani, G., et al. 2017a, *A&A*, 602, A2
- Smolčić, V., Novak, M., Bondi, M., et al. 2017b, *A&A*, 602, A1
- Smolčić, V., Schinnerer, E., Zamorani, G., et al. 2009, *ApJ*, 690, 610
- Stalevski, M., Fritz, J., Baes, M., Nakos, T., & Popović, L. Č. 2012, *MNRAS*, 420, 2756
- Stalevski, M., Ricci, C., Ueda, Y., et al. 2016, *MNRAS*, 458, 2288
- Tasse, C., Shimwell, T., Hardcastle, M. J., et al. 2021, *A&A*, 648, A1
- Uchiyama, H., Yamashita, T., Nagao, T., et al. 2022, *ApJ*, 934, 68
- Vaddi, S., O'Dea, C. P., Baum, S. A., et al. 2016, *ApJ*, 818, 182
- van der Vlugt, D., Hodge, J. A., Algera, H. S. B., et al. 2022, *ApJ*, 941, 10
- Wang, T., Elbaz, D., Alexander, D. M., et al. 2017, *A&A*, 601, A63
- Weaver, J. R., Kauffmann, O. B., Ilbert, O., et al. 2022, *ApJS*, 258, 11
- Weinberger, R., Springel, V., Hernquist, L., et al. 2017, *MNRAS*, 465, 3291
- Williams, R. J., Quadri, R. F., Franx, M., van Dokkum, P., & Labbé, I. 2009, *ApJ*, 691, 1879
- Williams, W. L. & Röttgering, H. J. A. 2015, *MNRAS*, 450, 1538
- Worpel, H., Brown, M. J. I., Jones, D. H., Floyd, D. J. E., & Beutler, F. 2013, *ApJ*, 772, 64
- Xie, F.-G. & Yuan, F. 2017, *ApJ*, 836, 104
- Xue, Y. Q., Luo, B., Brandt, W. N., et al. 2016, *ApJS*, 224, 15
- Yang, G., Boquien, M., Brandt, W. N., et al. 2022, *ApJ*, 927, 192
- Yang, G., Boquien, M., Buat, V., et al. 2020, *MNRAS*, 491, 740
- Yun, M. S., Reddy, N. A., & Condon, J. J. 2001, *ApJ*, 554, 803
- Zheng, X. C., Röttgering, H. J. A., van der Wel, A., & Duncan, K. 2022, *A&A*, 665, A114
- Zhu, S., Brandt, W. N., Zou, F., et al. 2023, *MNRAS*, 522, 3506

Appendix A: Spectral energy distribution (SED) fitting

CIGALE uses a series of AGN/galaxies templates to efficiently model the observed multi-wavelength data from the X-rays and far-ultraviolet (FUV) to the far-infrared (FIR) and radio bands. Through the Bayesian-like approach, this code estimates many fundamental physical properties, such as star formation rate, stellar mass, dust luminosity, AGN contribution and other quantities. In the fitting process, the galaxy templates used in this work includes the following six modules: the star formation history, the single stellar population (Bruzual & Charlot 2003), the dust attenuation (Calzetti et al. 2000), the dust emission (Dale et al. 2014), and the AGN module (Stalevski et al. 2012, 2016). These modules and their parameters are summarized in Table A.1. In Fig. A.1, we present the best-fit SEDs of four radio sources in the GOODS-N field as examples.

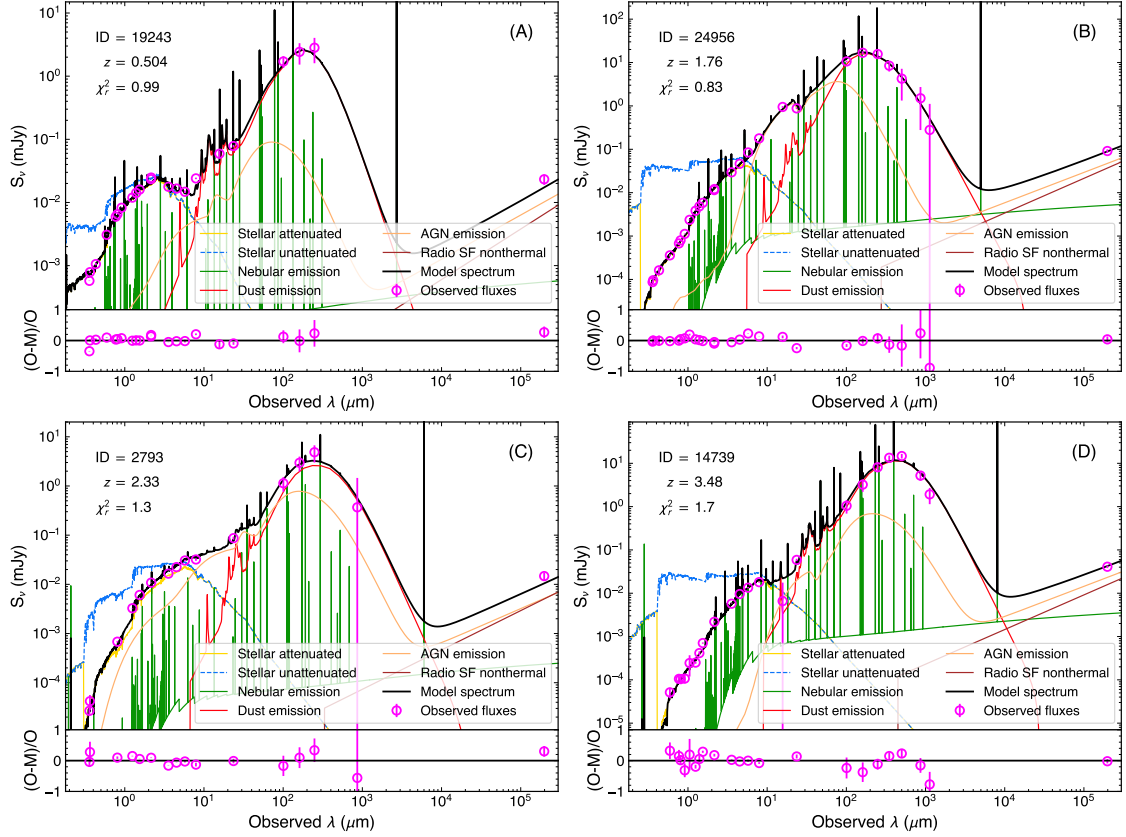


Fig. A.1: The best-fit SED model from CIGALE fitting for four radio sources as examples. Panels (A), (B), (C), and (D) show radio sources from the GOODS-N field with redshift z of 0.504, 1.76, 2.33, and 3.48, respectively.

Table A.1: Model parameters for SED fitting with CIGALE

Module	Parameter	Symbol	Values
Star formation history [$\text{SFR} \propto t \exp(-t/\tau)$]	Stellar e -folding time	$\tau_{\text{star}} (10^6 \text{ yr})$	50, 100, 250, 500, 1000, 2500, 5000, 10000
	Stellar age	$t_{\text{star}} (10^6 \text{ yr})$	100, 250, 500, 1000, 2500, 5000, 10000
Single stellar population (Bruzual & Charlot 2003)	Initial mass function	—	Chabrier (2003)
	Metallicity	Z	0.02
Dust attenuation (Calzetti et al. 2000)	Color excess of the nebular lines	$E(B - V) \text{ (mag)}$	0.005, 0.05, 0.1–0.7 (step 0.1), 0.9, 1.1, 1.3, 1.5
Galactic dust emission (Dale et al. 2014)	Slope in $dM_{\text{dust}} \propto U^{-\alpha} dU$	α	1.25, 1.5, 1.75, 2.0, 2.25, 2.5, 2.75
AGN (UV-to-IR)	AGN contribution to IR luminosity	frac_{AGN}	0.0, 0.01, 0.1, 0.3, 0.5, 0.7, 0.9, 0.99
	Viewing angle	θ	30°, 70°
	Polar-dust color excess	$E(B - V)_{\text{PD}} \text{ (mag)}$	0.0, 0.2, 0.4
Radio	SF radio-IR correlation parameter	q_{IR}	2.58
	Radio-loudness parameter	R_{AGN}	0.0, 0.01, 0.1, 1, 10, 100, 1000, 10000

Appendix B: Correct the classification purity for the radio-excess AGN

We use the cross point between the highest and the second highest gaussian components of q_{TIR} distribution as the threshold to select radio-excess AGN (see details in Section 4.1). Radio-excess AGNs with q_{TIR} around the selection threshold (corresponds to the q_{AGN} in Fig. 3 and the vertical black dash-dotted lines in Fig. B.1) are partially contaminated by the SFGs. To correct the classification purity for radio-excess AGN, we follow Delvecchio et al. (2022) to define f_{AGN} as the $1 - N_{\text{SFG}}/N_{\text{TOT}}$, where N_{SFG} represents the best-fit gaussian model for the highest q_{TIR} peak (see the highest dotted curves in Fig. B.1), and N_{TOT} represents the best-fit model for the entire q_{TIR} distribution (see the entire purple solid curves in Fig. B.1). At the threshold q_{AGN} (see the black dash-dotted line in Fig. B.1), f_{AGN} is usually below 50% for samples in the COSMOS field, while f_{AGN} is around 100% for the GOODS-N field. It indicates that the Radio-excess AGN Sample in the GOODS-N have a nearly 100% AGN purity under the selection threshold used in this work. Therefore, we only make AGN purity corrections for the objects in the COSMOS fields. Following Delvecchio et al. (2022), we use the $L_{1.4\text{GHz}}$ threshold converted from the median IR luminosity in each redshift bin to make the purity corrections.

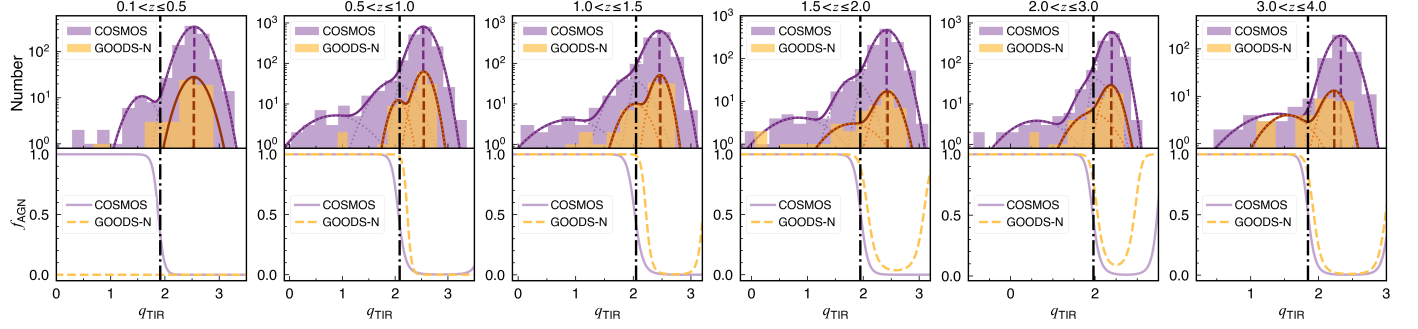


Fig. B.1: *Upper row*: Distribution of IR-radio-ratio (q_{TIR}) for SFGs in the GOODS-N (yellow histogram) and COSMOS/UltraVISTA (violet histogram) fields at different redshift bins (from left to right columns). Each dotted curve represents each single gaussian model, while the solid curve represents the best-fit model to the entire q_{TIR} distribution. The vertical dashed line corresponds to the peak position of the highest gaussian component. The vertical black dash-dotted line represents the threshold used in this work to separate SFGs and radio-excess AGNs (corresponds to q_{AGN} in Fig. 3 and see details in Section 4.1). *Bottom row*: Fraction of radio-excess AGNs in all the radio objects for the GOODS-N (yellow dashed curve) and COSMOS field/UltraVISTA (violet dashed curve) fields. Parameter f_{AGN} is defined as $1 - N_{\text{SFG}}/N_{\text{TOT}}$, where N_{SFG} represents the height of the highest gaussian model (the highest dotted curve) at a certain q_{TIR} value, and N_{TOT} represents the height of the entire best-fit model (entire solid curve) at a certain q_{TIR} value. The vertical black dash-dotted line represents the threshold used in this work to separate SFGs and radio-excess AGNs (same as the upper panels).

Appendix C: Radio luminosity function in each field: GOODS-N and COSMOS/UltraVISTA fields

We obtain the radio luminosity function in each field following the same procedure described in Section 5. For both SFGs and radio-excess AGNs, RLFs in these three fields present generally consistent results (see detailed discussions in Section 5).

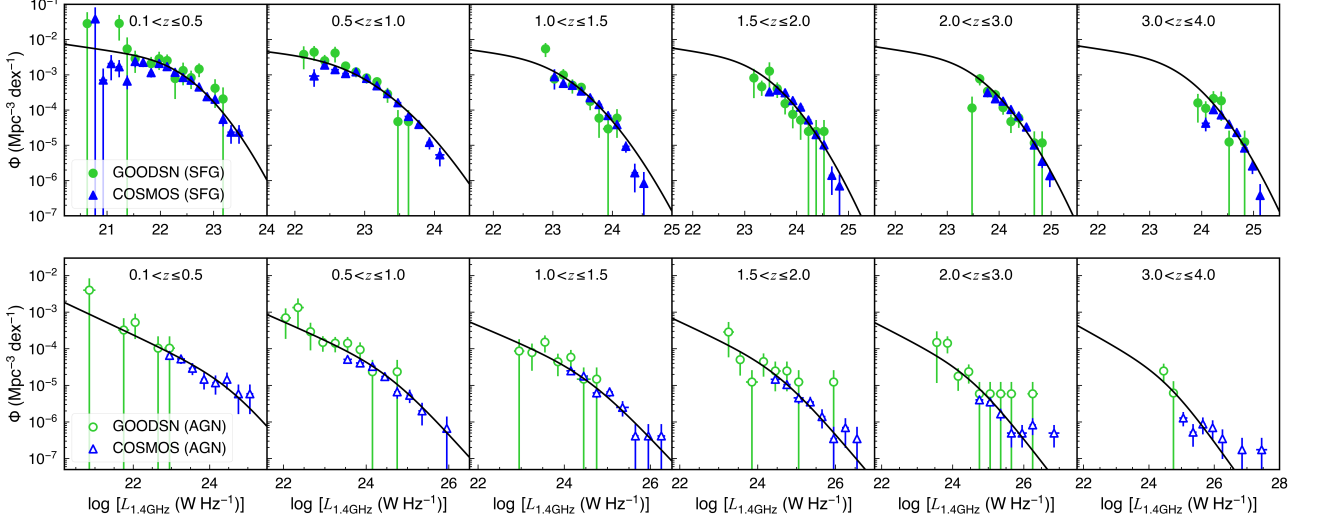


Fig. C.1: The 1.4 GHz Radio luminosity function of SFGs (*top row*) and radio-excess AGNs (*bottom row*) in each field (green circles: GOODS-N; blue triangles: COSMOS/UltraVISTA). The black solid curves in the *top row* represent the best-fit model (PLE) for SFGs. The black solid curves in the *bottom row* represent the best-fit model (PDE) for radio-excess AGNs.

Appendix D: Tables of radio luminosity functions for SFGs and radio-excess AGNsTable D.1: Radio luminosity function of SFGs obtained with the $1/V_{\max}$ method.

$\log L_{1.4\text{GHz}}$ [W Hz ⁻¹]	$\log \Phi$ [Mpc ⁻³ dex ⁻¹]	N	$\log L_{1.4\text{GHz}}$ [W Hz ⁻¹]	$\log \Phi$ [Mpc ⁻³ dex ⁻¹]	N	$\log L_{1.4\text{GHz}}$ [W Hz ⁻¹]	$\log \Phi$ [Mpc ⁻³ dex ⁻¹]	N
0.1 < z ≤ 0.5			0.5 < z ≤ 1.0			1.0 < z ≤ 1.5		
21.07 ± 0.05	-2.68 ± 0.28	4	22.12 ± 0.03	-2.42 ± 0.26	4	22.88 ± 0.03	-2.26 ± 0.17	16
21.22 ± 0.02	-1.81 ± 0.27	12	22.27 ± 0.04	-2.57 ± 0.15	14	23.02 ± 0.03	-3.08 ± 0.14	43
21.38 ± 0.02	-3.18 ± 0.16	9	22.43 ± 0.02	-2.66 ± 0.10	54	23.18 ± 0.02	-3.10 ± 0.11	162
21.52 ± 0.04	-2.58 ± 0.15	28	22.57 ± 0.03	-2.55 ± 0.14	135	23.32 ± 0.02	-3.30 ± 0.09	282
21.68 ± 0.04	-2.65 ± 0.10	48	22.72 ± 0.03	-2.84 ± 0.06	213	23.47 ± 0.03	-3.40 ± 0.07	297
21.82 ± 0.03	-2.79 ± 0.13	45	22.88 ± 0.02	-2.92 ± 0.06	332	23.62 ± 0.02	-3.70 ± 0.08	222
21.97 ± 0.02	-2.60 ± 0.13	82	23.02 ± 0.02	-3.09 ± 0.06	377	23.77 ± 0.02	-3.99 ± 0.09	157
22.12 ± 0.03	-2.67 ± 0.11	124	23.18 ± 0.02	-3.25 ± 0.07	299	23.93 ± 0.04	-4.15 ± 0.05	79
22.27 ± 0.03	-3.01 ± 0.13	133	23.32 ± 0.03	-3.54 ± 0.09	204	24.07 ± 0.03	-4.31 ± 0.19	46
22.43 ± 0.03	-2.96 ± 0.16	125	23.47 ± 0.04	-3.79 ± 0.04	115	24.22 ± 0.05	-5.03 ± 0.13	11
22.57 ± 0.03	-3.11 ± 0.12	111	23.62 ± 0.04	-4.18 ± 0.06	47	24.38 ± 0.04	-5.78 ± 0.31	2
22.72 ± 0.03	-3.02 ± 0.13	80	23.77 ± 0.03	-4.41 ± 0.08	29			
22.88 ± 0.04	-3.62 ± 0.07	39	23.93 ± 0.03	-4.92 ± 0.14	9			
23.02 ± 0.02	-3.51 ± 0.21	35	24.07 ± 0.05	-5.27 ± 0.22	4			
23.18 ± 0.04	-4.26 ± 0.14	9						
23.32 ± 0.05	-4.63 ± 0.22	4						
23.47 ± 0.05	-4.63 ± 0.22	4						
1.5 < z ≤ 2.0			2.0 < z ≤ 3.0			3.0 < z ≤ 4.0		
23.18 ± 0.06	-3.09 ± 0.31	2	23.62 ± 0.05	-3.11 ± 0.13	13	23.93 ± 0.04	-3.80 ± 0.31	2
23.32 ± 0.05	-3.34 ± 0.18	6	23.77 ± 0.02	-3.48 ± 0.07	96	24.07 ± 0.03	-4.11 ± 0.17	12
23.47 ± 0.03	-3.10 ± 0.24	73	23.93 ± 0.03	-3.62 ± 0.08	211	24.22 ± 0.03	-3.80 ± 0.16	81
23.62 ± 0.02	-3.41 ± 0.10	230	24.07 ± 0.03	-3.83 ± 0.06	317	24.38 ± 0.04	-3.89 ± 0.22	120
23.77 ± 0.03	-3.63 ± 0.07	283	24.22 ± 0.03	-4.12 ± 0.07	226	24.52 ± 0.03	-4.40 ± 0.05	81
23.93 ± 0.03	-3.88 ± 0.08	208	24.38 ± 0.03	-4.19 ± 0.09	176	24.68 ± 0.04	-4.63 ± 0.06	58
24.07 ± 0.03	-4.06 ± 0.09	162	24.52 ± 0.04	-4.48 ± 0.05	91	24.82 ± 0.04	-5.07 ± 0.09	22
24.22 ± 0.04	-4.28 ± 0.05	70	24.68 ± 0.04	-4.99 ± 0.08	30	24.97 ± 0.03	-5.58 ± 0.16	7
24.38 ± 0.03	-4.70 ± 0.08	27	24.82 ± 0.03	-5.45 ± 0.14	10			
24.52 ± 0.03	-4.99 ± 0.12	14	24.97 ± 0.03	-5.86 ± 0.22	4			

Notes. N is the source number in each luminosity bin.

Table D.2: Radio luminosity function of radio-excess AGNs obtained with the $1/V_{\max}$ method.

$\log L_{1.4\text{GHz}}$ [W Hz ⁻¹]	$\log \Phi$ [Mpc ⁻³ dex ⁻¹]	N	$\log L_{1.4\text{GHz}}$ [W Hz ⁻¹]	$\log \Phi$ [Mpc ⁻³ dex ⁻¹]	N	$\log L_{1.4\text{GHz}}$ [W Hz ⁻¹]	$\log \Phi$ [Mpc ⁻³ dex ⁻¹]	N
$0.1 < z \leq 0.5$			$0.5 < z \leq 1.0$			$1.0 < z \leq 1.5$		
22.05 ± 0.05	-3.28 ± 0.27	3	22.05 ± 0.11	-3.15 ± 0.31	2	23.25 ± 0.07	-4.10 ± 0.29	3
22.95 ± 0.06	-4.18 ± 0.09	12	22.35 ± 0.12	-2.87 ± 0.30	3	23.55 ± 0.05	-3.82 ± 0.20	19
23.25 ± 0.08	-4.27 ± 0.10	24	22.65 ± 0.03	-3.53 ± 0.29	3	23.85 ± 0.09	-4.35 ± 0.25	53
23.55 ± 0.08	-4.53 ± 0.14	22	22.95 ± 0.09	-3.83 ± 0.18	15	24.15 ± 0.05	-4.38 ± 0.15	62
23.85 ± 0.06	-4.83 ± 0.19	18	23.25 ± 0.06	-3.85 ± 0.18	45	24.45 ± 0.08	-4.74 ± 0.07	43
24.15 ± 0.06	-4.93 ± 0.22	11	23.55 ± 0.05	-4.01 ± 0.13	81	24.75 ± 0.07	-5.20 ± 0.11	16
24.45 ± 0.03	-4.83 ± 0.19	6	23.85 ± 0.05	-4.17 ± 0.15	65	25.05 ± 0.06	-5.17 ± 0.11	16
24.75 ± 0.05	-5.23 ± 0.31	4	24.15 ± 0.06	-4.48 ± 0.06	49	25.35 ± 0.13	-5.60 ± 0.18	6
25.05 ± 0.07	-5.23 ± 0.31	5	24.45 ± 0.07	-4.76 ± 0.09	26			
			24.75 ± 0.05	-5.17 ± 0.14	10			
			25.05 ± 0.06	-5.27 ± 0.15	8			
			25.35 ± 0.07	-5.70 ± 0.25	3			
$1.5 < z \leq 2.0$			$2.0 < z \leq 3.0$			$3.0 < z \leq 4.0$		
23.25 ± 0.12	-3.54 ± 0.34	3	23.55 ± 0.08	-3.83 ± 0.40	2	24.45 ± 0.07	-4.60 ± 0.22	4
23.55 ± 0.08	-4.29 ± 0.27	3	23.85 ± 0.07	-3.84 ± 0.20	9	25.05 ± 0.10	-5.89 ± 0.16	4
24.15 ± 0.01	-4.35 ± 0.26	8	24.15 ± 0.04	-4.75 ± 0.25	8	25.35 ± 0.08	-6.28 ± 0.25	7
24.45 ± 0.08	-4.70 ± 0.19	30	24.45 ± 0.07	-4.63 ± 0.22	23	25.65 ± 0.06	-6.06 ± 0.19	3
24.75 ± 0.04	-4.75 ± 0.22	42	24.75 ± 0.09	-5.39 ± 0.09	23	25.95 ± 0.03	-6.15 ± 0.22	5
25.05 ± 0.11	-5.34 ± 0.12	33	25.05 ± 0.06	-5.45 ± 0.09	21	26.25 ± 0.05	-6.45 ± 0.31	4
25.35 ± 0.07	-5.45 ± 0.14	13	25.35 ± 0.05	-5.78 ± 0.14	10			
25.65 ± 0.07	-5.85 ± 0.22	10	25.65 ± 0.10	-6.30 ± 0.25	3			
26.25 ± 0.07	-6.15 ± 0.31	4	25.95 ± 0.11	-6.30 ± 0.25	3			
			26.25 ± 0.07	-6.08 ± 0.19	5			
			26.85 ± 0.13	-6.30 ± 0.25	3			

Notes. N is the source number in each luminosity bin.

Appendix E: Radio luminosity function for radio-excess AGN split into the subsets hosted by SFGs and QGs

We obtain the radio luminosity function for radio-excess AGN hosted by different populations (SFGs and QGs) following the same procedure described in Section 5. We found a similar evolution trend for radio-excess AGN hosted by different populations to that for low-excitation radio galaxies in [Kondapally et al. \(2022\)](#) (see detailed discussions in Section 5.3).

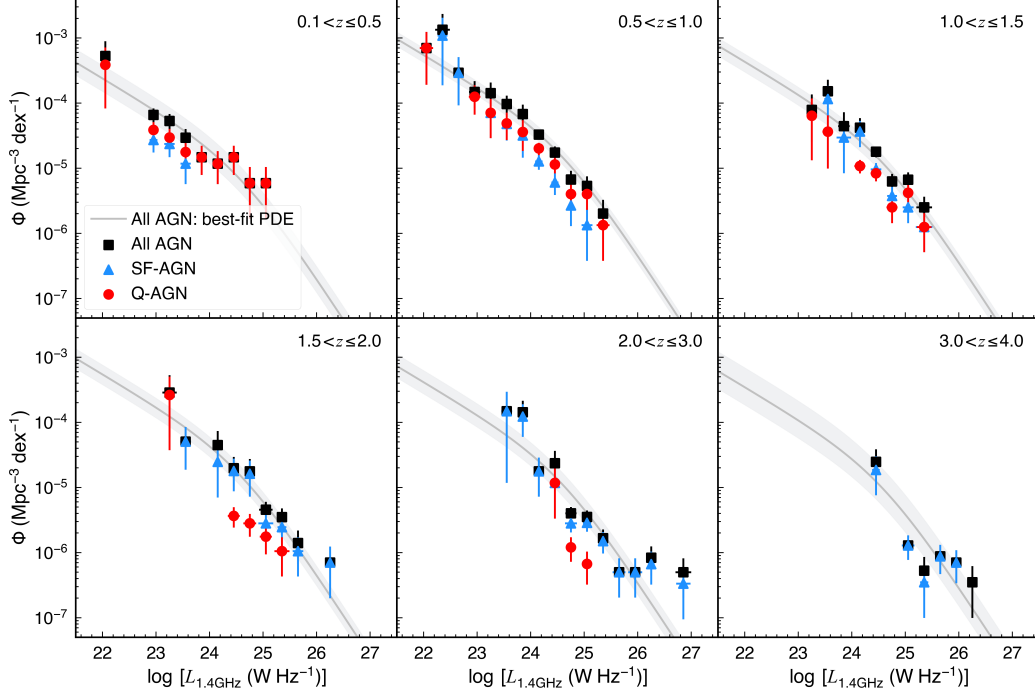


Fig. E.1: The 1.4 GHz Radio luminosity function of all the radio-excess AGNs (black squares) split into the subsets hosted by SFGs (blue triangles) and QGs (red circles). The grey solid curves represent the best-fit PDE model for all the radio-excess AGNs and the grey regions represent the $1\text{-}\sigma$ uncertainty of the best-fit model.

Appendix F: Simple χ^2 fits to the probability of hosting a radio-excess AGN in each redshift bin

As Equation 22 or 23 shows, at each fixed L_R (or M_\star), we assume a simple power-law relation for $p(L_R | M_\star, z)$ as a function of M_\star (or L_R). Then we apply χ^2 fits to the data (see colored symbols in Fig. F.1 and Fig. F.2). The best-fit model in each L_R (or M_\star) bin is shown as the colored line in the left column of Fig. F.1 (or Fig. F.2). The best-fit parameters in each L_R (or M_\star) bin are shown as colored points in the right column of Fig. F.1 (or Fig. F.2). For more details about analysis and discussion, we refer readers to Section 6.3.3.

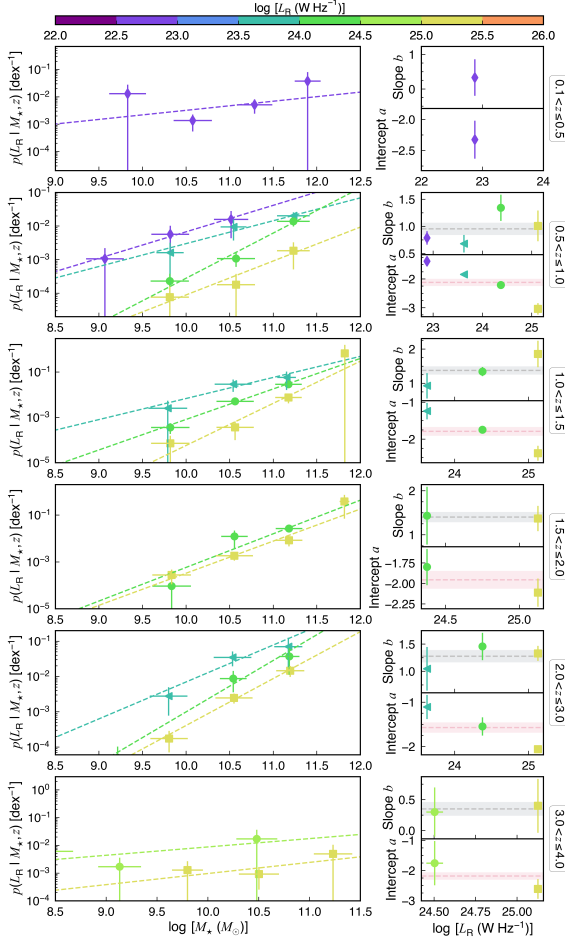


Fig. F.1: *Left column:* The probability density function $p(L_R | M_\star, z)$ of a SFG hosting a radio-excess AGN with a given 1.4 GHz luminosity L_R as a function of stellar mass M_\star at different redshift bins (from upper to bottom rows). Different colors represent different L_R bins. Each dashed line represents the best-fit power-law relation for $p(L_R | M_\star, z)$ as a function of M_\star in each L_R bin (defined by Equation 22). *Right column:* Best-fit slope b (upper panel at each redshift bin) and intercept a (bottom panel at each redshift bin) of the above power-law relation. Different colors represent different L_R bins (same as those in the left column). In the upper-right panel of each redshift bin, the gray dashed line shows the mean of slopes over all the L_R bins (\bar{b}), while the gray region represents $\bar{b} \pm 0.1$. In the bottom-right panel of each redshift bin, the pink dashed line shows the mean of intercepts over all the L_R bins (\bar{a}), while the pink region represents $\bar{a} \pm 0.1$. The region scale (± 0.1) is just a reference value for showing the difference between each data point with the mean value.

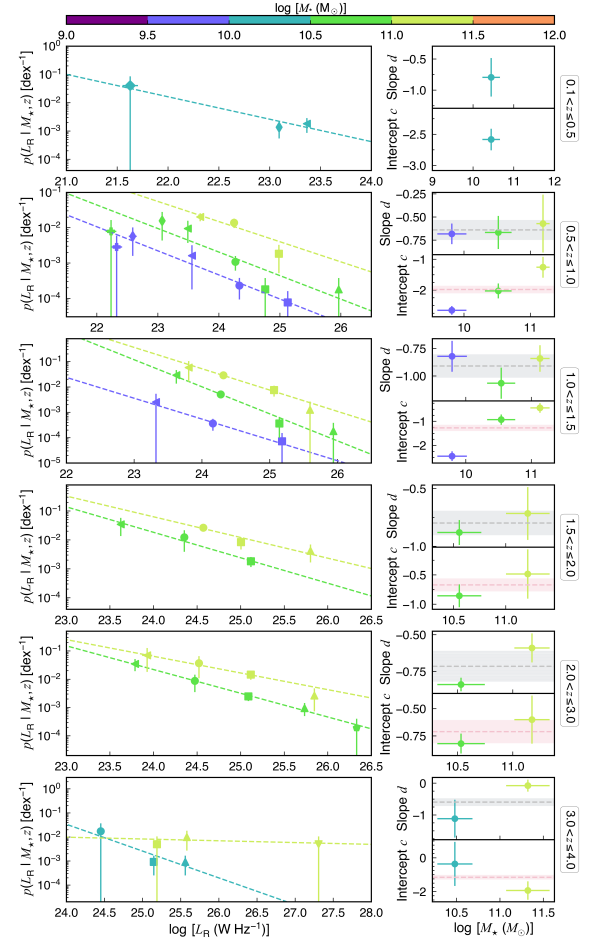


Fig. F.2: *Left column:* The probability density function $p(L_R | M_\star, z)$ of a SFG with a given stellar mass M_\star hosting a radio-excess AGN as a function of 1.4 GHz luminosity L_R at different redshift bins (from upper to bottom rows). Different colors represent different M_\star bins. Each dashed line represents the best-fit power-law relation for $p(L_R | M_\star, z)$ as a function of L_R in each M_\star bin (defined by Equation 23). *Right column:* Best-fit slope d (upper panel at each redshift bin) and intercept c (bottom panel at each redshift bin) of the above power-law relation. Different colors represent different M_\star bins (same as the left column). In the upper-right panel of each redshift bin, the gray dashed line shows the mean of slopes over all the M_\star bins (\bar{d}), while the gray region represents $\bar{d} \pm 0.1$. In the bottom-right panel of each redshift bin, the pink dashed line shows the mean of intercepts over all the M_\star bins (\bar{c}), while the pink region represents $\bar{c} \pm 0.1$. The region scale (± 0.1) is just a reference value for showing the difference between each data point with the mean value.

Appendix G: The probability of hosting a radio-excess AGN in QGs and all the galaxies

Similar to Section 6.3 (mainly for SFGs), here we show the probability of hosting a radio-excess AGN in QGs and all the galaxies based on maximum-likelihood fitting over the entire redshift range.

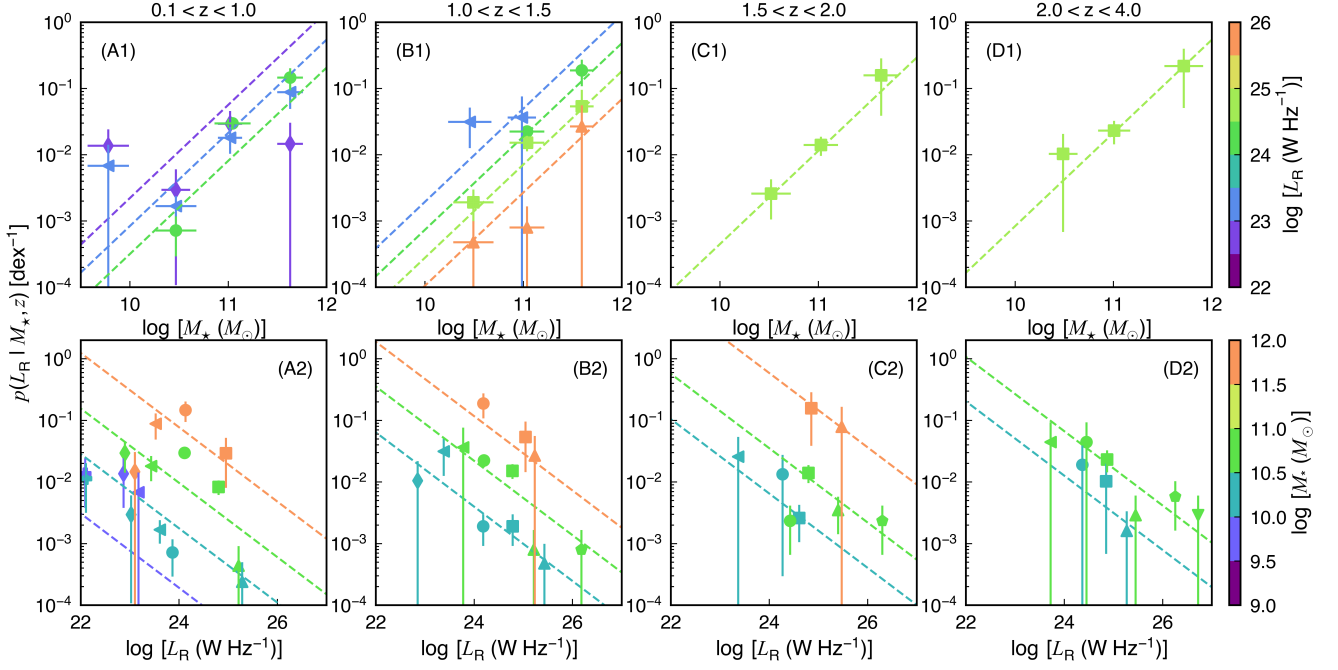


Fig. G.1: Estimates of $p(L_R | M_*, z)$ as a function of M_* and L_R based on our maximum-likelihood fitting results for QGs. Colored dashed lines in both top and bottom rows represent our best-fit model from the unbinned maximum-likelihood fitting (see Equation 28 and Table 2) through combining data in the three fields (GOODS-N and COSMOS/UltraVISTA) over the entire redshift range ($0.1 < z < 4$) evaluated at the center of each redshift bin. Binned data points are scaled with the probability estimated by the model (see Equation 28) using the $N_{\text{obs}}/N_{\text{mdl}}$ method of Aird et al. (2012) (see details in Section 6.3.3). In the top panel, different colors represent different M_* bins. In the bottom panel, different colors indicate different L_R bins.

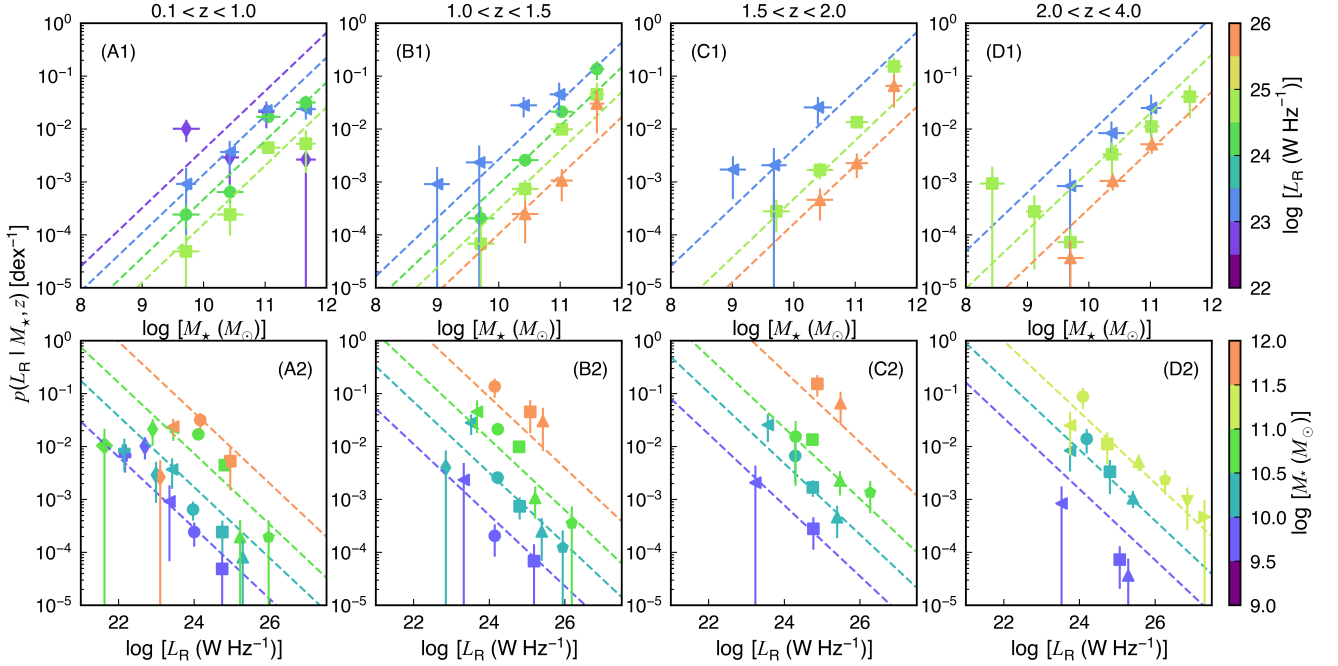


Fig. G.2: Same as Fig. 8 and Fig. G.1 but for all galaxies.

Appendix H: The evolution of $p(L_R | M_*, z)$ in SFGs considering the M_* -dependent IRRC

In order to examine whether the M_* -dependent IRRC will affect our results, we follow [van der Vlugt et al. \(2022\)](#) to select radio-excess AGNs with q_{TIR} deviating more than 3σ from the M_* -dependent IRRC of [Delvecchio et al. \(2021\)](#). To compare with the results shown in Section 6.3 (see the green region in Fig. H.1), we also use Equation 28 to recalculate the probability of SFGs hosting a radio-excess AGN (see the dark blue region in Fig. H.1). Fig. H.1 shows that using the M_* -dependent IRRC ([Delvecchio et al. 2021](#)) does not alter the results in this work.

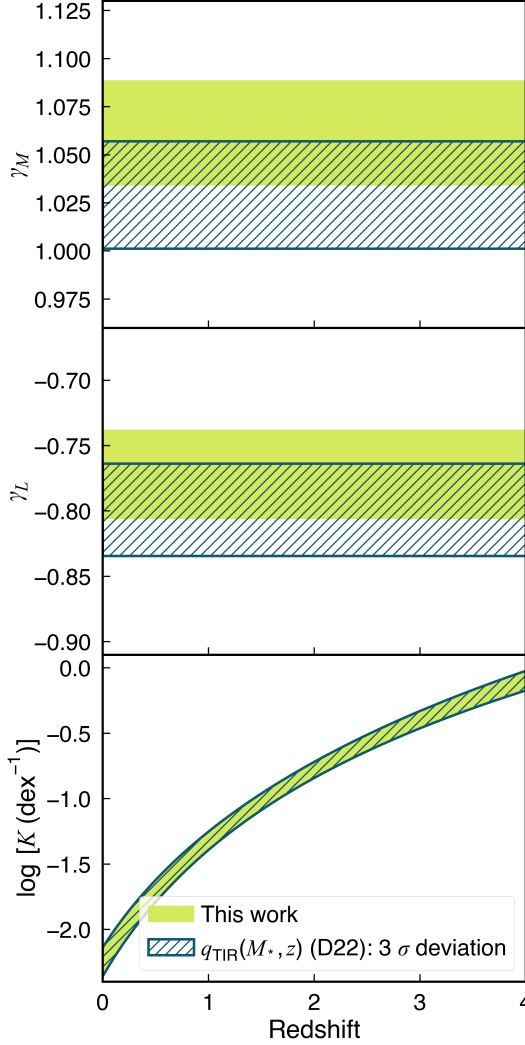


Fig. H.1: Best-fit parameters of the maximum-likelihood fitting for $p(L_R | M_*, z)$ in SFGs over the entire redshift range. Green regions correspond to the best-fit parameters based on the sample selected by the method in Section 4 (same as the blue region in Fig. 7). Dark blue regions correspond to the best-fit parameters based on the sample selected by the M_* -dependent IRRC ([Delvecchio et al. 2021](#), see details in Section 7).